NUMERICAL HEAT TRANSFER, PART A
2017, VOL. 72, NO. 8, 600–627
https://doi.org/10.1080/10407782.2017.1394134

Taylor & Francis
Taylor & Francis Group

Natural convection of power-law fluids under wall vibrations: A lattice Boltzmann study

Jian-Fei Xie and Bing-Yang Cao

Key Laboratory for Thermal Science and Power Engineering of Ministry of Education, Department of Engineering Mechanics, Tsinghua University, Beijing, China

ABSTRACT

The natural convection of non-Newtonian power-law fluids in a rectangular cavity in the presence of wall vibrations has been investigated by the lattice Boltzmann method. The longitudinal and transverse vibrations are applied to the horizontal walls of the cavity separately, and the two vertical walls are set as high and low temperatures, respectively. The velocity fields and temperature distributions of power-law fluids are visualized with respect to the streamlines and isotherm contours. The heat transfer characteristics are interpreted in terms of averaged Nusselt number ($\overline{Nu}$) near the surface of heated wall. The effects of power-law index n in the range of 0.5–1.2 on momentum transport and heat transfer are investigated for Rayleigh number (Ra) in the range of 10^3–10^5 and Prandtl number (Pr) of 10. $\overline{Nu}$ near the hot wall is increased significantly with the fluid exponent increase at high Ra, but it is smaller than that without wall vibrations. Moreover, wall vibrations show slight and even no influence on $\overline{Nu}$ of power-law fluids at low Ra. The maximum velocity components of shear-thinning fluids are both decreased under wall vibrations with increasing n, but it is unchanged in shear-thickening fluids. The velocity components along the central lines of the cavity are decreased significantly for power-law fluids under wall vibrations. It is concluded that wall vibrations influence the streamlines, isotherm contours, and heat transfer characteristics of power-law fluids significantly at high Ra ($\sim 10^5$). In addition, it has been found that the heat transfer rate is decreased as both aspect ratio and Pr increase.

ARTICLE HISTORY
Received 5 May 2017
Accepted 10 October 2017

1. Introduction

Flows of Newtonian and non-Newtonian fluids driven by buoyancy in rectangular enclosures are found in a wide range of engineering applications such as nuclear reactors, solar devices, food products, and polymer processing industries [1]. For differentially heated two-dimensional enclosures with adiabatic side walls, the heat transfer characteristics are influenced by the inclination of cavity with respect to the horizontal plane, Prandtl number, and Rayleigh number based on the height of the cavity. For example, Vinogradov et al. [2] investigated the steady natural convection of both Newtonian and non-Newtonian shear-thickening liquids confined in rectangular cavities with different aspect ratios and found significant variation in heat transfer rate. On the other hand, most structured fluids of polymeric and/or multiphase nature encountered in industrial practice exhibit the shear-thinning behavior which is characterized by an apparent viscosity and can vary as a function of the shear rate by several orders of magnitudes. Instinctively, this dependence of viscosity upon the shear rate further accentuates the coupling between the velocity and temperature fields due to the

CONTACT Bing-Yang Cao caoby@tsinghua.edu.cn Key Laboratory for Thermal Science and Power Engineering of Ministry of Education, Department of Engineering Mechanics, Tsinghua University, Beijing 100084, China.
Color versions of one or more of the figures in the article can be found online at www.tandfonline.com/unht.

Nomenclature

$\mathbf{c}$	discrete particle velocity
k	consistency of fluid
c_s	speed of sound
n	fluid exponent
$\dot{e}$	local shear rate
$\overline{Nu}$	averaged Nusselt number
e	strain rate
Pr	Prandtl number
$\mathbf{f}$	buoyancy force
R	gas constant
F	body force
Ra	Rayleigh number
f	density distribution function
T	temperature
$\mathbf{g}$	gravity
t	time
G	pressure gradient
$\mathbf{u}$	fluid velocity
g	temperature distribution function
V^*	reference velocity
H	height of cavity
$\mathbf{x}$	particle coordinate

Greek symbols

α	thermal diffusion coefficient
ρ	fluid density
β	thermal expansion coefficient
τ	relaxation time
δ	expansion parameter
μ	dynamic viscosity
ε	internal energy
ν	kinematic viscosity

Superscripts

eq	equilibrium state
neq	nonequilibrium state

Subscripts

c	temperature index
s	speed index
eff	effective
ν	density index
i	discrete direction

point to point variation of the fluid viscosity in the flow domain, thereby influencing the rate of heat transfer in an intricate manner [3].

External factors and varying boundary conditions may influence the heat transfer characteristics of natural convection of fluids [4–6]. For example, the effect of a magnetic field on natural convection of non-Newtonian power-law fluids in a cavity with a linearly heated wall had been analyzed by a finite difference lattice Boltzmann method [7], and the entropy generation caused by the natural convection in an enclosure filled with non-Newtonian nanofluids had also been simulated [8, 9]. Results indicated that the augmentation of power-law index in the absence of magnetic field results in a decrease in heat transfer, and the increment of the magnetic field power declines the effect of power-law index on heat transfer. Moreover, laminar mixed convection of shear-thinning fluids in a square lid-driven cavity with sinusoidal boundary conditions under the combined buoyancy effects of thermal and mass diffusion had also been analyzed [10, 11], including the sinusoidal temperature profile. The fall of the power-law index declines the heat and mass transfer at small Richard numbers. However, for unity of Richard number, the heat and mass transfer rise with the increment of power-law index for buoyancy ratio of unity.

Non-Newtonian fluid flows are usually complicated and require much pumping energy to drive the fluid flowing through tube lines and processing equipment, so that various ways of facilitating their flow and processing have been sought over the past decades [12–14]. Mechanical vibration can result in the fluidity of the material and hence facilitate its processing [15–18]. Particularly, Eesa and Barigou [19] reported a computational fluid dynamics investigation into the effects of rotational oscillation on the flow rate of four types of fluids: Newtonian, power law, Herschel–Bulkley, and Bingham plastic, in a straight tube. In the last two decades, after the pioneering work [20, 21], the rapid growth of LBM for physical flows has been seen obviously [22–24] and great efforts have been made in incompressible thermal flows [25, 26], high-frequency oscillating flows [27], phase separation in thin fluid films [28, 29], and microscale oscillating flows in microelectromechanical systems [30]. Particularly, Aharonov and Rothman [31] proposed the first LBM model for the power-law fluids. In this model, the relaxation time in the BGK collision term varies as a function of shear stress at each time step to give the local fluid viscosity that depends on the strain-rate tensor. One decade later, an *ad hoc* modification of this LBM model was introduced by Gabbanelli et al. [32], i.e., a truncated power-law model, to overcome the limits of viscosity divergence and zero-viscosity for shear-thinning

and shear-thickening fluids, respectively. Recently, advanced lattice Boltzmann schemes of non-Newtonian fluids have been developed including: integrated lattice Boltzmann and finite volume method to modeling incompressible polymer viscoelastic fluid flows [33], mass-conserving lattice Boltzmann model [34], decoupling multiple-relaxation-time lattice Boltzmann flux solver [35], and free-energy-based LBM for multiphase fluids with possible high-density and high-viscosity ratios [36]. Moreover, Yoshino et al. [37] constructed a novel lattice Boltzmann model for the inelastic non-Newtonian fluids. Shortly the model has been modified and applied to Bingham plastic materials and blood flow by Wang et al. [38, 39]. In addition, the immersed boundary-LBM (IB-LBM) has been introduced to simulate the non-Newtonian fluid flows with applications to stationary/moving objects with various shapes [40], unconfined flow and heat transfer [41, 42], and harmonic oscillations of lamina in power-law fluids [43].

The early studies, however, are limited to narrow ranges of vibration conditions and rheological behaviors. Although the fruitful progress has been reached in the study of non-Newtonian fluids, a fundamental understanding of the physical changes that may occur in the product during vibration and a quantitative description of their effects on its rheological behavior of natural convection is still less understood. Our purpose in this paper is to find such information and it is organized as follows. In Section 2, we present a lattice Boltzmann scheme to modeling the non-Newtonian power-law fluids, including both momentum and temperature evolutions. Section 3 formulates the natural convection of non-Newtonian power-law fluids and the boundary conditions, including the nonequilibrium extrapolation scheme and the description of wall vibrations. The code validation and mesh independence are investigated in Section 4. In Section 5, the natural convection of both power-law and Newtonian fluids confined in a rectangular cavity with two vertical walls vibrating along the longitudinal and transverse directions is investigated by the LBM model, respectively. Conclusions are drawn in Section 6.

2. Mathematical model

2.1. Lattice Boltzmann equations

In this paper, we choose a square lattice in two dimensions [44] to evolve the flow, which is shown in Figure 1. The lattice Boltzmann equation can be viewed as an implementation of the Boltzmann

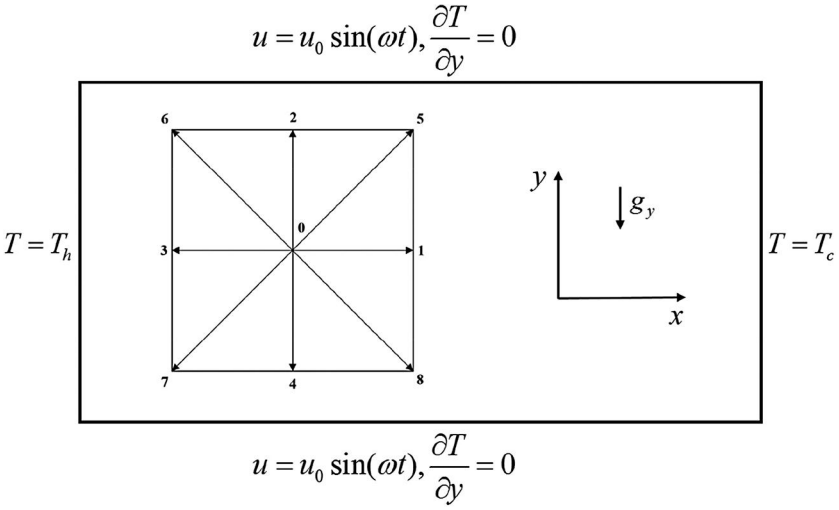

Figure 1. Heat boundary condition for natural convection in a rectangular cavity with vibrating walls. D2Q9 multispeed model is applied and the two components of the lattice velocity are $\mathbf{c}_{ix} = \{0, 1, 0, -1, 0, -1, -1, -1, 1\}$ and $\mathbf{c}_{iy} = \{0, 0, 1, 0, -1, 1, 1, -1, -1\}$, $i = 0$–8, respectively.

equation on a discrete lattice and for a discrete set of velocity distribution functions. The BGK lattice Boltzmann equation that is discretized in both space and time is given by

$$f_i(\mathbf{x}+\mathbf{c}_i\Delta t, t+\Delta t) - f_i(\mathbf{x},t) = \frac{1}{\tau_\nu}\left(f_i(\mathbf{x},t) - f_i^{\mathrm{eq}}(\mathbf{x},t)\right) + \Delta t F_i, \tag{1}$$

where $\mathbf{x}$ and t are the space coordinate and time, Δt is the time step, τ_ν is the relaxation time that controls the rate of approach to equilibrium, and F_i is the body force. In addition, the discrete velocity $\mathbf{c}_i$ is defined as follows [45]:

$$\mathbf{c}_i = \begin{cases} (0,0), \ i=0; \\ (\cos\theta_i, \sin\theta_i), \theta_i = (i-1)\frac{\pi}{2}, \ i=1-4; \\ \sqrt{2}(\cos\theta_i, \sin\theta_i), \theta_i = (i-5)\frac{\pi}{2}+\frac{\pi}{4}, \ i=5-8. \end{cases} \tag{2}$$

f_i ($\mathbf{x}$, t) is the density distribution function and its equilibrium state f_i^{eq} ($\mathbf{x}$, t) is given by

$$f_i(\mathbf{x},t)^{\mathrm{eq}} = \begin{cases} \frac{4}{9}\rho\left(1-\frac{3}{2}u^2\right), i=0; \\ \frac{4}{9}\rho\left[1+3(\mathbf{c}_i\cdot\mathbf{u})+\frac{9}{2}(\mathbf{c}_i\cdot\mathbf{u})^2-\frac{3}{2}u^2\right], \ i=1-4; \\ \frac{4}{36}\rho\left[1+3(\mathbf{c}_i\cdot\mathbf{u})+\frac{9}{2}(\mathbf{c}_i\cdot\mathbf{u})^2-\frac{3}{2}u^2\right], \ i=5-8. \end{cases} \tag{3}$$

The fluid density ρ and velocity $\mathbf{u}$ can be obtained by

$$\rho = \sum_i f_i; \ \rho\mathbf{u} = \sum_i f_i\mathbf{c}_i. \tag{4}$$

The relaxation time τ_ν is related to the kinematic viscosity ν of the fluid as follows

$$\nu = \frac{(2\tau_\nu - 1)}{6}, \tag{5}$$

The macroscopic governing equations can be recovered by the Chapman–Enskog expansion approach [46, 47].

2.2. Lattice Boltzmann scheme for non-Newtonian fluids

For non-Newtonian fluids, the effective viscosity μ_{eff} is applied, which varies with the local shear rate $\dot{e}$. Here the shear rate $\dot{e}$ is taken as the second invariant of the symmetric strain rate $e_{\alpha\beta}$ as follows [48]:

$$\dot{e} = \sqrt{e_{\alpha\beta}e_{\alpha\beta}}, \tag{6}$$

with

$$e_{\alpha\beta} = \frac{1}{2}\left(\frac{\partial u_\beta}{\partial x_\alpha} + \frac{\partial u_\alpha}{\partial x_\beta}\right), \tag{7}$$

where u is the fluid velocity, subscripts α and β represent the component index in Cartesian coordinates, and the summation convention is used hereafter. The power-law relationship in non-Newtonian fluids is considered and the effective viscosity is given by [39]

$$\mu_{\mathrm{eff}} = k\dot{e}^{n-1}, \tag{8}$$

where k and n are fluid parameters: k is a measurement of consistency of the fluid, and larger values of k refer to more viscous fluids; n is a measurement of degree of non-Newtonian behavior, and the greater departure from unity is pronounced in the more non-Newtonian properties of the fluid [48]. The case $n<1$ corresponds to the shear-thinning (pseudo-plastic) fluids, $n>1$ corresponds to the shear-thickening (dilatant) fluids, and $n=1$ recovers the Newtonian behavior, respectively. The consistency index can be linked with the relaxation time of the Newtonian fluid by a relation similar to Eq. (5), since it can be regarded as the viscosity of the fluid when $n=1$. Other types

of non-Newtonian fluids such as Herschel–Bulkley and Bingham plastic materials and viscoplastic materials are not considered in the present work, and more details about these fluids can be referred to [19, 49–51] and references cited herein.

As described above, for the power-law fluids, the effective viscosity μ_{eff} is a function of local shear rate $\dot{e}$, i.e., the viscosity is related to the local rate of strain through the constitutive equation for the shear stress tensor. Therefore, the kinetic viscosity related to the relaxation time τ_v cannot remain invariable, and one has to model the non-Newtonian fluid by determining the value of relaxation time locally. In what follows, we extend the lattice Boltzmann scheme to model the non-Newtonian fluids, in which the power-law relationship between the effective viscosity and the local shear strains is applied to deduce the local effective viscosity. The numerical algorithm is proposed below:

i. First of all, the lattice nodes are initialized with the desired density and velocity on the basis of the fluid properties.
ii. Then the shear rate $\dot{e}$ is calculated from the velocity field in terms of $\mathbf{u} = \sum_i f_i \mathbf{c}_i / \rho$.
iii. With the shear rate $\dot{e}$ known, one can compute the effective viscosity μ_{eff} using Eq. (8), which can be rewritten as follows [9, 52]:

$$\mu_{eff} = k\left\{2\left[\left(\frac{\partial u}{\partial x}\right)^2 + \left(\frac{\partial v}{\partial y}\right)^2\right] + \left(\frac{\partial v}{\partial x} + \frac{\partial u}{\partial y}\right)^2\right\}^{\frac{n-1}{2}}, \tag{9}$$

where u and v are the velocity components along the x and y directions, respectively. Clearly, for a Newtonian fluid $n = 1$, μ_{eff} reduces to the conventional viscosity.

iv. Evolving the population of distribution functions on the nodes of the square lattice with respect to the relaxation time τ_v, properties of the fluid will be updated using Eq. (4).
v. Return to step (ii) with the updated fluid density and velocity until a steady flow state has been reached.

It should be noted that the shear stress $\dot{e}$ is calculated locally in the present algorithm. The symmetric strain rate $e_{\alpha\beta}$ can also be calculated locally at each node of the lattice as follows [53]:

$$e_{\alpha\beta} = -\frac{3}{2\tau_v}\sum_i f_i^{(1)} \mathbf{c}_i \mathbf{c}_i, \tag{10}$$

where $f_i^{(1)}$ is the first-order term of the non-equilibrium distribution function as it is further expanded. The terms $f_i^{(1)}$ are usually calculated as part of the velocity calculations in the lattice Boltzmann equations. Thus obtaining the shear stress using Eq. (10) is sufficiently efficient than calculating the space derivatives of the fluid velocity.

2.3. Internal energy distribution

For the evolution of temperature in natural convection, the temperature distribution function is given by:

$$g_i(\mathbf{x} + \mathbf{c}_i\Delta t, t + \Delta t) - g_i(\mathbf{x}, t) = \frac{1}{\tau_c}\left(g_i(\mathbf{x}, t) - g_i^{\text{eq}}(\mathbf{x}, t)\right) \tag{11}$$

where τ_c is the relaxation time for temperature distribution function g_i ($\mathbf{x}$, t) and g_i^{eq} ($\mathbf{x}$, t) is the equilibrium distribution of temperature. The equilibrium states of the temperature distribution functions are defined as follows:

$$g(\mathbf{x}, t)^{\text{eq}} = \begin{cases} -\frac{\rho\varepsilon}{2}u^2, i = 0; \\ \frac{\rho\varepsilon}{18}\left[1 + \mathbf{c}_i \cdot \mathbf{u} + \frac{9}{2}(\mathbf{c}_i \cdot \mathbf{u})^2 - \frac{3}{2}u^2\right], \ i = 1 - 4; \\ \frac{\rho\varepsilon}{36}\left[1 + 4\mathbf{c}_i \cdot \mathbf{u} + \frac{9}{2}(\mathbf{c}_i \cdot \mathbf{u})^2 - \frac{3}{2}u^2\right], \ i = 5 - 8. \end{cases} \tag{12}$$

The internal energy $\varepsilon = 3RT/2$ can be calculated by [54]

$$\rho\left(\frac{3RT}{2}\right) = \sum_i g_i, \tag{13}$$

where R and T are the gas constant and the fluid temperature, respectively, and the thermal diffusion coefficient is defined as $\alpha = \frac{9}{5}(\tau_c - 12)$.

Then we expand the temperature distribution function g_i with respect to $g_i^{(0)}$ as follows

$$g_i = g_i^{(0)} + \delta g_i^{(1)} + \delta^2 g_i^{(2)} + O(\delta^3), \tag{14}$$

The first-order expansion of Eq. (11) is

$$(\partial_{t0} + \mathbf{c}_i \cdot \nabla) g_i^{(0)} = -\frac{1}{\tau_c} g_i^{(1)}, \tag{15}$$

and the second-order expansion of Eq. (11) is

$$\partial_{t1} g_i^{(0)} + \left(1 - \frac{1}{2\tau_c}\right)(\partial_{t0} + \mathbf{c}_i \cdot \nabla) g_i^{(1)} = -\frac{1}{\tau_c} g_i^{(2)}. \tag{16}$$

Summing Eqs. (15) and (16) using the distribution of the internal energy, respectively, we have

$$\partial_{t0}(\rho\varepsilon) + \nabla \cdot (\rho \mathbf{u} \varepsilon) = 0, \tag{17}$$

and

$$\partial_{t1}(\rho\varepsilon) + \left(1 - \frac{1}{2\tau_c}\right)\Pi^{(1)} = 0, \tag{18}$$

where $\Pi^{(1)} = \sum_i (\partial_{t0} + \mathbf{c}_i \cdot \nabla) g_i^{(1)}$, and particularly $\Pi^{(1)} = -\tau_c \frac{9}{5} \nabla^2 (\rho\varepsilon)$ when omitting $O(u^2 \delta T)$. Combining Eqs. (17) and (18), the energy equation can be recovered as follows

$$\partial_t(\rho\varepsilon) + \nabla \cdot (\rho \mathbf{u} \varepsilon) = \alpha \nabla^2 (\rho\varepsilon). \tag{19}$$

3. Problem formation

3.1. Natural convection of power-law fluids

The natural convection of power-law fluids with the fluid exponent n in the range of 0.5–1.2 is performed using the lattice Boltzmann scheme, which has been proposed for non-Newtonian fluids in Section 2. The flow configuration consists of a two-dimensional rectangular cavity with a hot vertical wall on the left and a cold vertical wall on the right, as shown in Figure 1, and the horizontal (bottom and top) walls are considered to be perfectly insulated.

The two dimensionless parameters, Rayleigh number (Ra) and Prandtl number (Pr), which characterize the natural convective flow, are defined as follows

$$Ra = \frac{g\beta\Delta T H^3}{\nu\alpha}, \quad Pr = \frac{\nu}{\alpha}, \tag{20}$$

where g is the gravitational acceleration, β is the thermal expansion coefficient, ΔT is the temperature difference between the two vertical walls, and H is the height (half of the width) of the cavity. In the following simulations, $Ra = 10^3$, 10^4, 10^5 and $Pr = 10$ are set unless stated otherwise, and we apply the Boussinesq approximation to confine the power-law fluids to be laminar flow in the rectangular cavity [55]. Moreover, the assumptions that viscous dissipation, radiation, chemical reaction, and temperature dependency of the fluid viscosity are negligible in the energy equation are made. The buoyancy force $\mathbf{f}$ is directly proportional to the temperature variation as follows

$$\mathbf{f} = -\rho T_0 \mathbf{g}\beta(T - T_0) \tag{21}$$

where $T_0 = (T_h + T_c)/2$ is the reference temperature. The body force applied to the momentum transport, i.e., Eq. (1), can be given by:

$$F_i = \frac{\mathbf{f} \cdot (\mathbf{c}_i - \mathbf{u})}{RT} f_i^{eq}, \tag{22}$$

We also consider the averaged heat transfer rate through the hot vertical wall $\overline{Nu}$, the maximum vertical velocity V_{max}/V^* along the horizontal center line, and the maximum horizontal velocity U_{max}/V^* along the vertical center line. Correspondingly $\overline{Nu}$ and V^* are defined as [26]

$$\overline{Nu} = -\frac{1}{\Delta T}\sum_{1}^{H}(\partial_x T)_{x=0}, V^* = \frac{\nu}{PrH} \tag{23}$$

3.2. Boundary conditions

In our simulations, no-slip velocity condition is imposed on the rigid walls of the cavity. As shown in Figure 1, fixed temperatures (Dirichlet conditions) are prescribed on the vertical walls (T_h and T_c), whereas the horizontal walls are perfectly insulated (Neumann conditions), i.e., $\partial T/\partial y = 0$. For the adiabatic horizontal walls, i.e., nontemperature gradient condition, we implement this condition as follows. The temperatures of fluids and the two horizontal walls are set the averaged value of the hot vertical wall and cold vertical wall temperatures initially. During the evolution of temperature distributions, the temperature of fluids has been updated, and the temperatures of horizontal walls are taken the same values as the fluid temperature that is next to the corresponding wall. The perfectly insulted walls are therefore implemented. The bounce-back condition is generally used to deal with the density distribution function on the rigid walls and is casting doubt on their applicability to other boundary conditions including a combination of density, velocity, temperature, and their derivatives [56]. A nonequilibrium extrapolation scheme is thus introduced [57, 58] and can be used for both steady and unsteady flow in theory. It is also found that the nonequilibrium extrapolation exhibits better numerical stability. In this paper, the nonequilibrium extrapolation scheme is applied to both density and temperature distribution functions on the walls, which is shown in Figure 2.

On the basis of nonequilibrium extrapolation scheme, the distribution function is split into two parts

$$f_i(O,t) = f_i^{eq}(O,t) + f_i^{neq}(O,t), \tag{24}$$

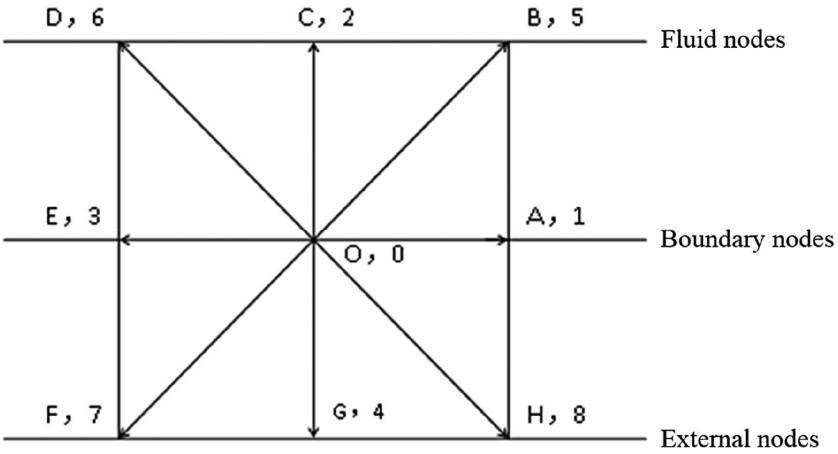

Figure 2. Nonequilibrium extrapolation scheme for a D2Q9 multispeed model.

In the meantime, we define a dummy equilibrium distribution as follows

$$\overline{f_i^{\mathrm{eq}}}(O,t) = E_i(\rho(C,t), \mathbf{u}(O,t)) \tag{25}$$

and the equilibrium state of distribution function is given by:

$$f_i^{\mathrm{eq}} = E_i(\rho, \mathbf{u}) = \omega_i \rho \left[1 + \frac{\mathbf{c}_i \cdot \mathbf{u}}{c_s^2} + \frac{(\mathbf{c}_i \cdot \mathbf{u})^2}{2c_s^4} - \frac{u^2}{2c_s^2}\right] \tag{26}$$

where c_s is the speed of sound and is chosen as $c_s = 1/\sqrt{3}$. Based on Eq. (24), we can get the nonequilibrium state of distribution function

$$f_i^{\mathrm{neq}}(C,t) = f_i(C,t) - f_i^{\mathrm{eq}}(C,t), \tag{27}$$

Substituting Eqs. (25) and (27) into Eq. (24), we obtain the distribution function at the boundary

$$f_i(O,t) = \overline{f_i^{\mathrm{eq}}}(O,t) + [f_i(C,t) + f_i^{\mathrm{eq}}(C,t)]. \tag{28}$$

Therefore, the distribution functions of density and temperature on the walls can be given by

$$\begin{aligned} f_{i,\mathrm{wall}} &= \overline{f_{i,\mathrm{wall}}^{\mathrm{eq}}} + f_{i,\mathrm{wall}} - f_{i,\mathrm{fluid}}^{\mathrm{eq}} \\ g_{i,\mathrm{wall}} &= \overline{g_{i,\mathrm{wall}}^{\mathrm{eq}}} + g_{i,\mathrm{wall}} - g_{i,\mathrm{fluid}}^{\mathrm{eq}}, \end{aligned} \tag{29}$$

where $\overline{f_{i,\mathrm{wall}}^{\mathrm{eq}}}$ and $\overline{g_{i,\mathrm{wall}}^{\mathrm{eq}}}$ are the dummy equilibrium distributions on the wall, which are determined by Eqs. (3) and (12) along with the no-slip velocity condition, and their densities are equal to those of fluid nodes (B, C, and D) that are close to the wall nodes (A, O, and E). It should be noted that Eq. (28) is also valid for nodes A B and E D. In addition, $f_{i,\mathrm{wall}}^{\mathrm{eq}}$ and $g_{i,\mathrm{wall}}^{\mathrm{eq}}$ are the equilibrium distributions of density and temperature on the fluid nodes next to the walls, respectively. It is known that the nonequilibrium extrapolation scheme requires some information from the inside flow regions, indicating that the treatment is of second-order accuracy at each boundary node. This kind of treatment is different from the bounce-back condition, where each calculation is restricted only to the local nodes.

We now introduce the application of wall vibration, and as shown in Figure 1, the sinusoidal forcing wall displacements are imposed to the top and bottom walls of the rectangular cavity [59]. We perform the natural convection of viscous power-law fluids in the cavity illustrated in Figure 1, and both longitudinal and transverse vibrations are considered. Consequently, the velocity of the moving wall under the longitudinal (transverse) vibration is demonstrated by $u = u_0 \cdot \sin\omega t$ ($v = v_0 \cdot \sin\omega t$) with $\omega = 2\pi/T$, where u_0 (v_0), ω, and T are the amplitude, frequency, and period of the vibration, respectively. The values or ranges of physical parameters used in our LBM simulations are shown in Table 1, and it should be noted that the kinematic viscosity is a variable and can be derived from the effective viscosity which is dependent on the local shear rate. It is known that the good hydrodynamic behavior can be achieved for $\tau_v < 1$, whereas the poor hydrodynamic behavior may be seen for $\tau_v > 1$ [60]. Moreover, Niu et al. [61] had investigated the stability and hydrodynamics of different lattice Boltzmann models and found that all the LBM approaches seem unstable for $\tau_v << 0.5$. In the previous work, Eggels and Somers [62] set the kinematic viscosity in

Table 1. Values or ranges of key physical parameters in the present LBM simulations.

Parameter	Symbol	Value
Kinematic viscosity	ν	0.0005–0.2
Relaxation time for mass	τ_v	0.5015–1.1
Fluid consistency	k	0.01–5.0
Fluid exponent	n	0.5–1.2
Prandtl number	Pr	0.71–10^2
Relaxation time for temperature	τ_c	0.5009–0.536
Rayleigh number	Ra	10^3–10^6

LBM, lattice Boltzmann method.

the range of $0.00001 < \nu < 0.25$ in lattice Boltzmann simulation of free convective flow, and Gabbanelli et al. [32] set the lower and upper saturation values of the kinematic viscosity in their truncated power-law model to $\nu_{min} = 0.001$ and $\nu_{max} = 0.1$. The chosen values or ranges of variables in the present LBM simulations can guarantee the reasonable hydrodynamic behaviors and numerical stability.

4. Code validation and mesh independence

Based on the lattice Boltzmann scheme of the non-Newtonian fluids introduced in Section 2.2, we present the results of the planar pressure-driven Poiseuille flow with respect to the pressure boundary condition [63], which are shown in Figure 3. It should be noted that the fluid variables and parameters used in the simulation are set by the lattice units. To validate our LBM solver, the analytical solution for the power-law fluid flow is also given by [39, 64]

$$u(y) = \left(\frac{n}{n+1}\right)\left(\frac{G}{\mu}\right)\left[\left(\frac{H}{2}\right)^{\frac{n+1}{n}} - |y|^{\frac{n+1}{n}}\right], \tag{30}$$

where G is the pressure gradient. It is seen in Figure 3 that for three values of fluid index, i.e., $n = 0.5$ ($k = 0.01$), 1.0 ($k = 0.1$), and 1.2 ($k = 1.0$), the velocity profiles obtained by our LBM solver reach a good agreement with the analytical solution. This agreement enables us to simulate the power-law fluid flow using the present LBM non-Newtonian solver. In addition, the treatment of surface vibration should be tested before we apply the vibrating wall condition to natural convections in the cavity. As an example, take the case of planar Couette flow driven by the top wall moving with

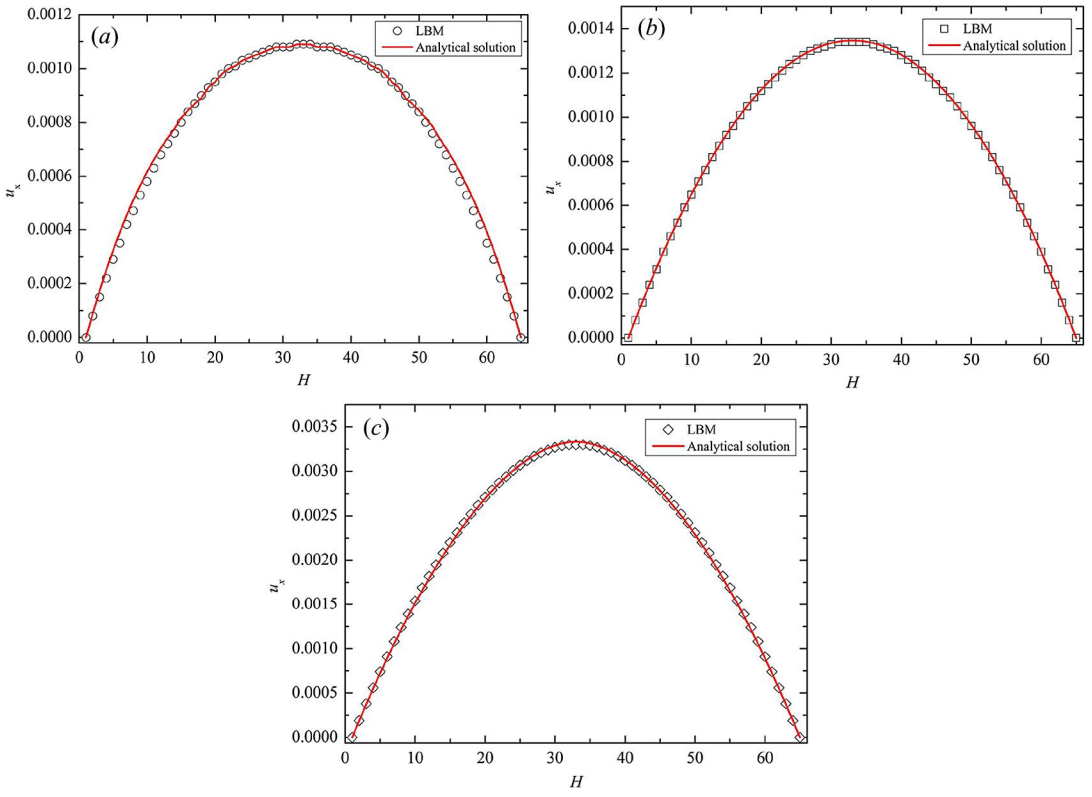

Figure 3. Velocity profiles of power-law Poiseuille flow for: (*a*) $n = 0.5$; (*b*) $n = 1.0$; and (*c*) $n = 1.2$. The solid red lines represent the analytical solution expressed in Eq. (30).

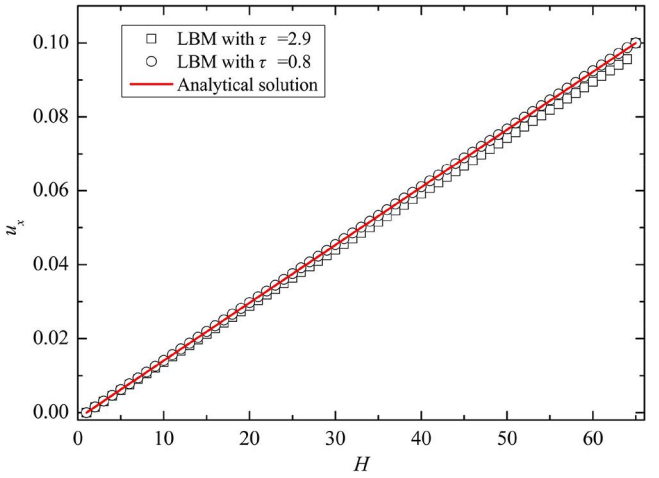

Figure 4. Velocity profiles of Couette flow: open squares and circles represent the LBM results with over-relaxation and under-relaxation times, respectively. The solid red line shows the analytical solution.

a constant velocity $u_0 = 0.1$ (the distance between top and bottom walls is 65 lattice units), and the periodic and velocity boundary conditions are applied to the inlet/outlet and walls, respectively. Two relaxation times are used in our LBM simulations, i.e., overrelaxation ($\tau = 2.9$) and underrelaxation ($\tau = 0.8$). As is seen in Figure 4, the result with the underrelaxation time reaches an excellent agreement with the analytical solution ($u(y) = u_0\, y/H$).

On the other hand, the natural convection in a square cavity has been performed to validate our thermal LBM solver, and the results are compared with the benchmark data and available results in the literature, which is shown in Table 2. The comparison in Table 2 indicates that our thermal LBM results reach a reasonable agreement with the benchmark data. As mentioned earlier, the nonequilibrium extrapolation scheme is applied to the evolution of both mass and temperature distributions on the walls, and the comparison between the nonequilibrium extrapolation scheme and bounce-back boundary condition has been made, which is also shown in Table 2. As shown in Table 2, the maximum velocity components obtained by the bounce-back boundary condition are close to these computed by the nonequilibrium extrapolation scheme and benchmark data. The averaged Nusselt number that characterizes the heat transfer rate, however, is underpredicted by the bounce-back

Table 2. Comparison of the averaged Nusselt number $\overline{Nu}$, the maximum velocity components along the central lines U_{max}/V^* and V_{max}/V^* with available results and benchmark data in the literature in a square cavity for $Ra = 10^4$–10^6, $Pr = 0.71$, and $n = 1.0$.

$Ra = 10^4$	$\overline{Nu}$	U_{max}/V^*	V_{max}/V^*
Present results with nonequilibrium extrapolation BC	2.2703	19.5648	16.1252
Present results with bounce-back BC	1.2552	19.7799	16.2906
Barakos et al.[70]	2.245	19.717	16.262
de Vahl Davis and Jones [71]	2.243	19.617	16.178
Fusegi [72]	2.302	18.959	16.937
$Ra = 10^5$	$\overline{Nu}$	U_{max}/V^*	V_{max}/V^*
Present results with nonequilibrium extrapolation BC	4.5528	68.3976	34.7521
Present results with bounce-back BC	2.5747	70.1897	35.6749
Barakos et al.[70]	4.51	68.746	35.173
de Vahl Davis and Jones [71]	4.519	68.59	34.73
Fusegi [72]	4.646	65.815	39.169
$Ra = 10^6$	$\overline{Nu}$	U_{max}/V^*	V_{max}/V^*
Present results with nonequilibrium extrapolation BC	8.5853	225.73219	65.7175
Present results with bounce-back BC	5.0944	238.1117	69.6346
Janssen [73]	8.8196	221.277	64.681
Le Quéré[74]	8.8259	220.408	64.796

Table 3. Mesh independence: The averaged Nusselt number $\overline{Nu}$, the maximum velocity components along the central lines U_{max}/V^* and V_{max}/V^* for $Ra = 10^3$, $Pr = 10$, and $n = 1.0$.

Mesh grid	$\overline{Nu}$	U_{max}/V^*	V_{max}/V^*
100×50	0.5071	0.9385	0.5902
110×55	0.5067	0.9421	0.5915
120×60	0.5063	0.9449	0.5945
130×65	0.5059	0.9474	0.5953
140×70	0.5057	0.9494	0.5973
150×75	0.5055	0.9511	0.5979

boundary condition for Ra ranged from 10^4 to 10^6. To demonstrate the mesh independence in our simulations, the dependence of numerical accuracy on the mesh grids has been investigated for the natural convection of Newtonian fluid in the rectangular cavity without wall vibrations using such meshes as 100×50, 110×55, 120×60, 130×65, 140×70, and 150×75. The numerical results of the averaged Nusselt number and the maximum velocity components along the central lines of the cavity with different mesh grids are shown in Table 3, which indicate the independence of numerical results on the mesh grid up to 130×65. Therefore, the following results and discussion are all based on the mesh grid 130×65.

5. Results and discussion

Temperature distributions of the natural convection of power-law fluids are shown in Figures 5–7 for longitudinal (x-direction) and transverse (y-direction) vibrations, respectively. It can be seen that

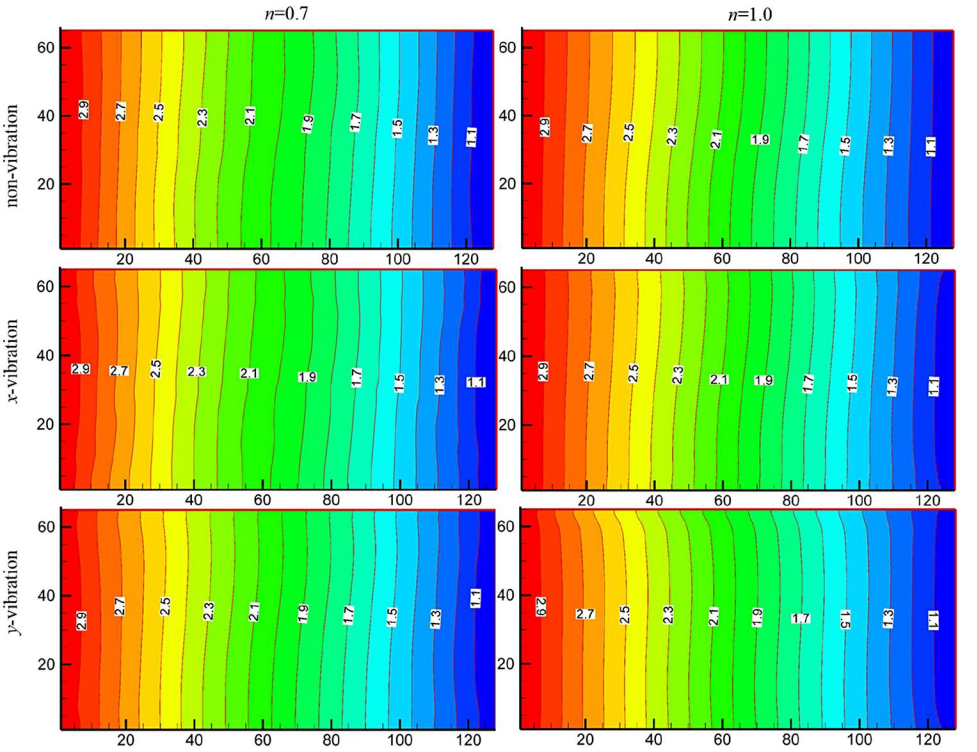

Figure 5. Temperature distributions of power-law fluids and Newtonian fluid in a rectangular cavity under the longitudinal and transverse vibrations ($Ra = 10^3$ and $Pr = 10$), respectively.

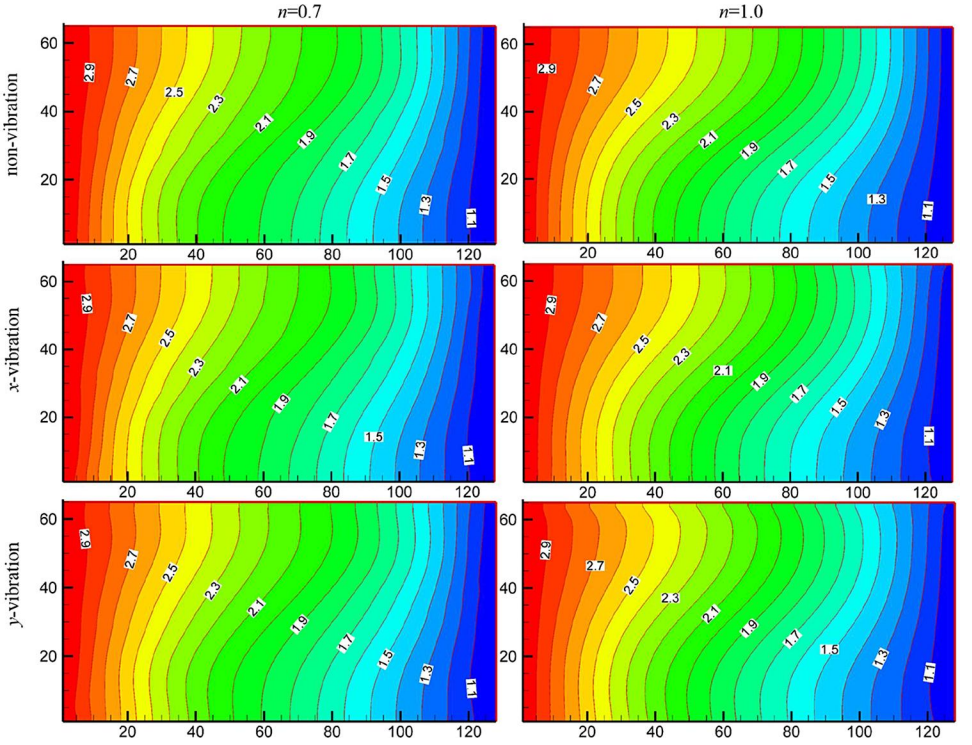

Figure 6. Temperature distributions of power-law fluids and Newtonian fluid in a rectangular cavity under the longitudinal and transverse vibrations ($Ra = 10^4$ and $Pr = 10$), respectively.

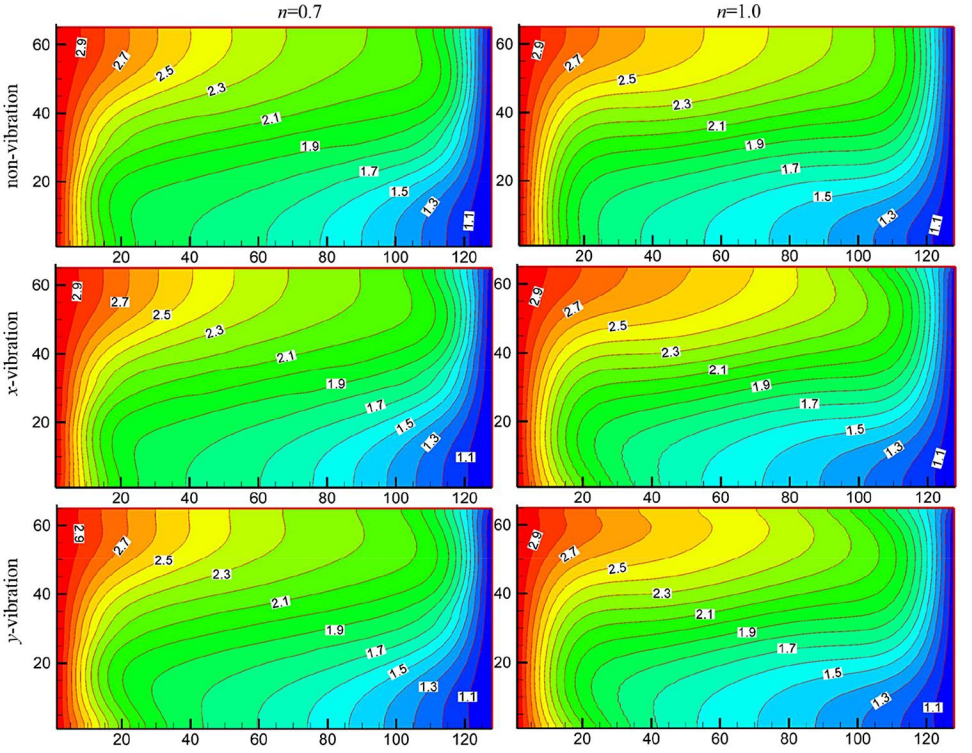

Figure 7. Temperature distributions of power-law fluids and Newtonian fluid in a rectangular cavity under the longitudinal and transverse vibrations ($Ra = 10^5$ and $Pr = 10$), respectively.

Table 4. Flow parameters: The averaged Nusselt number $\overline{Nu}$, the maximum velocity components along the central lines U_{max}/V^* and V_{max}/V^*, and the stream function $|\psi_{max}|$ for $Pr = 10$ under the longitudinal vibration of horizontal walls in a rectangular cavity.

	n	$\overline{Nu}$	$U_{max}/V*$	$V_{max}/V*$	$\lvert\psi_{max}\rvert$
$Ra = 10^3$	0.5	0.4447	0.7593	0.3269	0.036
	0.7	0.5389	1.1009	0.3492	0.007
	1.0	0.4928	11.1431	0.5587	0.0016
	1.2	0.5376	1.3752	1.0056	0.0016
$Ra = 10^4$	0.5	0.4824	4.3557	2.5976	0.14
	0.7	0.5078	6.8771	4.0187	0.036
	1.0	0.5931	12.3506	5.6991	0.008
	1.2	0.7267	11.6581	9.8265	0.022
$Ra = 10^5$	0.5	1.2343	12.8639	11.4662	0.2
	0.7	1.3716	26.6784	23.6375	0.1
	1.0	1.6328	32.2207	39.8809	0.034
	1.2	2.1528	38.2221	48.1955	0.13

temperature distributions are influenced under the longitudinal and transverse vibrations compared to the isothermal lines without wall vibrations. At low Ra such as 10^3 and 10^4, the isothermal lines in the cavity are not influenced by the wall vibrations significantly, which is shown in Figures 5 and 6. As Ra increases to 10^5, as shown in Figure 7, the natural convection is affected under the y-vibration more efficiently for both power-law and Newtonian fluids. Particularly, the isothermal lines are bended to the left on the top wall and bended to the right on the bottom wall, respectively. As shown in Table 4, the averaged Nusselt number $\overline{Nu}$ near the hot wall is increased for both power-law and Newtonian fluids under the x-vibration when Ra increases from 10^3 to 10^5. It is also seen in Table 5 that $\overline{Nu}$ is always increased under the y-vibration for both Newtonian and power-law fluids.

Flow fields of power-law fluids are shown in Figures 8–10 for longitudinal and transverse vibrations, respectively. For power-law fluid under the x-vibration at $Ra = 10^3$, as shown in Figure 8, the central main vortex is compressed down the center of the cavity and two secondary vortices are produced at the upper corners of the cavity. However, for the power-law fluid under y-vibration, the central main vortex is moved to left slightly, and two secondary vortices are produced near the hot and cool walls, respectively. On the other hand, for Newtonian fluid under the x-vibration, the cavity is occupied by an upper vortex and a lower vortex. But the cavity is occupied by a main vortex near the cool wall and a secondary vortex near the hot wall for Newtonian fluid under y-vibration. When Ra increases to 10^4, as shown in Figure 9, there are two smaller secondary vortices at the upper corners of the cavity under x-vibration and two smaller secondary vortices at the corners of cool wall under y-vibration, respectively. The similar phenomena appear for Newtonian fluid under both x and

Table 5. Flow parameters: The averaged Nusselt number $\overline{Nu}$, the maximum velocity components along the central lines U_{max}/V^* and V_{max}/V^*, and the stream function $|\psi_{max}|$ for $Pr = 10$ under the transverse vibration of horizontal walls in a rectangular cavity.

	n	$\overline{Nu}$	$U_{max}/V*$	$V_{max}/V*$	$\lvert\psi_{max}\rvert$
$Ra = 10^3$	0.5	0.5139	0.7544	0.4295	0.036
	0.7	0.5389	0.7299	1.9866	0.0035
	1.0	0.5589	3.0565	10.7013	0.002
	1.2	0.5066	0.9435	0.6659	0.0014
$Ra = 10^4$	0.5	0.5524	5.6339	3.5374	0.14
	0.7	0.5516	5.8135	3.9681	0.034
	1.0	0.6511	6.2689	9.0307	0.006
	1.2	0.7643	8.0975	7.3616	0.02
$Ra = 10^5$	0.5	1.2805	7.6249	6.8225	0.22
	0.7	1.2542	27.0022	23.1907	0.1
	1.0	1.6816	29.7187	39.3263	0.032
	1.2	2.2335	35.4849	45.7209	0.12

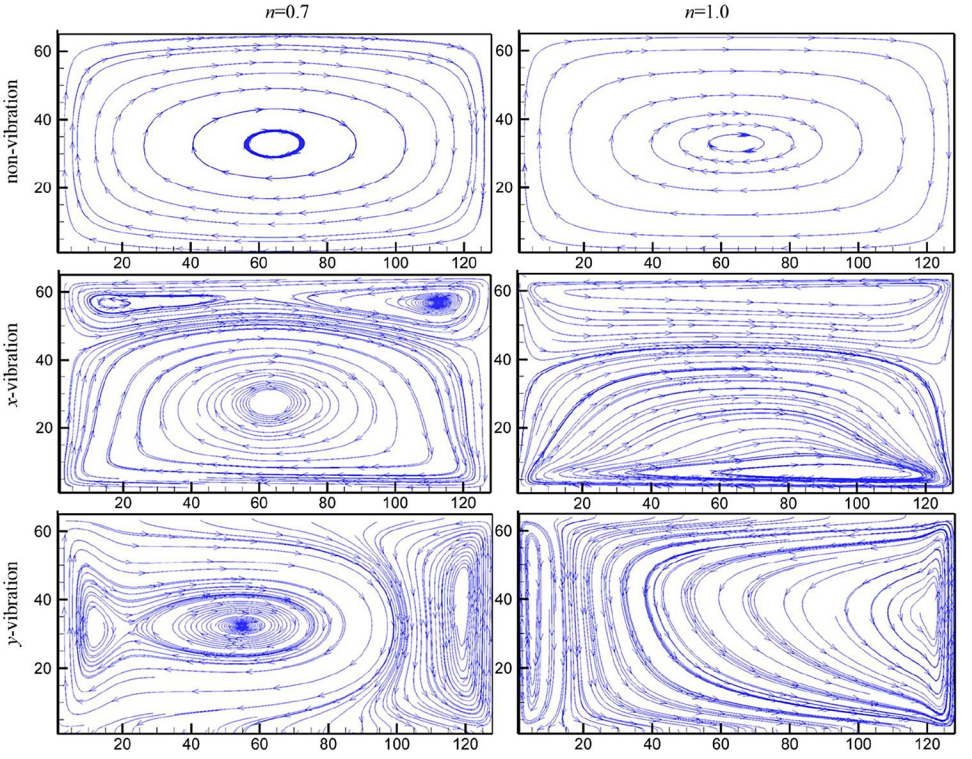

Figure 8. Velocity fields of power-law fluids and Newtonian fluid in a rectangular cavity under the longitudinal and transverse vibrations ($Ra = 10^3$ and $Pr = 10$), respectively.

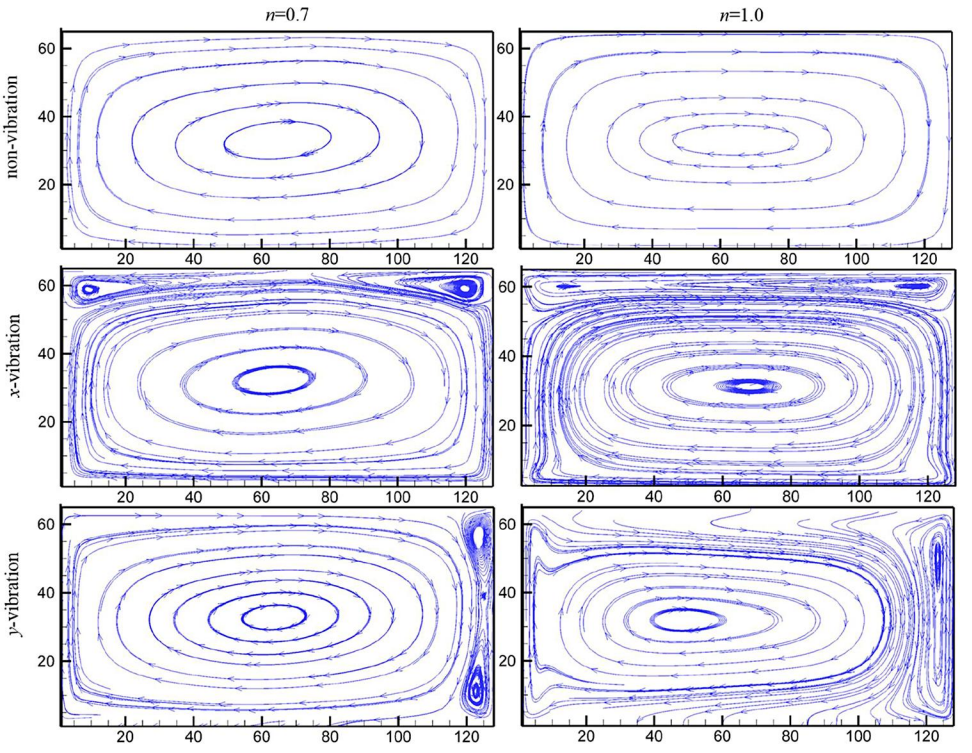

Figure 9. Velocity fields of power-law fluids and Newtonian fluid in a rectangular cavity under the longitudinal and transverse vibrations ($Ra = 10^4$ and $Pr = 10$), respectively.

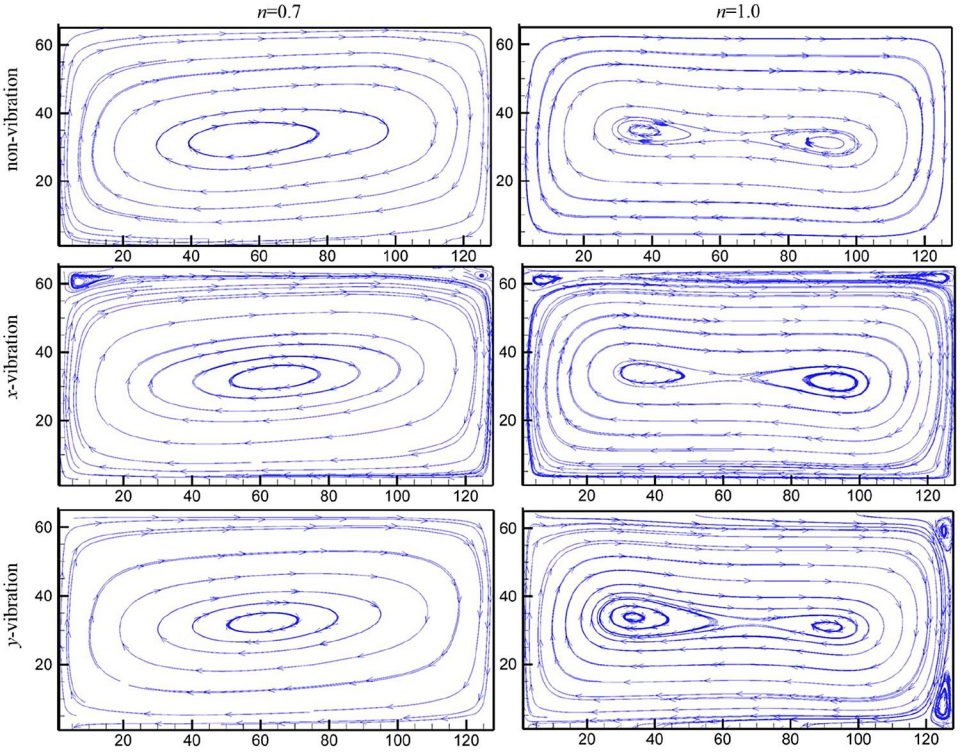

Figure 10. Velocity fields of power-law fluids and Newtonian fluid in a rectangular cavity under the longitudinal and transverse vibrations ($Ra = 10^5$ and $Pr = 10$), respectively.

y-vibrations, but the velocity traces are sharp at the bottom corners of the main vortex. When *Ra* increases to 10^5, as shown in Figure 10, the two secondary vortices get smallest under *x*-vibration for power-law fluid, and there are no secondary vortices appeared under the *y*-vibration. On the other hand, two secondary vortices are still produced for Newtonian fluid at the corners of top and right walls under both *x* and *y*-vibrations. Recently, Delouei et al. [41] have investigated the steady and unsteady flows over a cylinder for the shear-thinning, Newtonian, and shear-thickening fluids using the IB-LBM approach, respectively, and have found that the place and size of the vortex which is formed behind the cylinder are highly dependent on the fluid index. Moreover, the shedding vortex length is very sensitive to the fluid indices in steady flows, and the fluid index plays an important role in the separation phenomenon in unsteady flows. Therefore, mechanisms of the apparent viscosity of power-law fluids influenced by the fluid index have been explored, which is shown in Figure 11 for the shear-thinning fluid ($n = 0.7$). As is seen in Figure 11, the maximum viscosity of the shear-thinning fluid is distributed along the central lines of the rectangular cavity for $Ra = 10^3$, but the minimum viscosity is concentrated near the four corners. As *Ra* increases to 10^5, the area of maximum viscosity is enlarged in the center of cavity. However, the area of minimum viscosity has shrunk or disappeared near the four corners. Accordingly, the vortex that is formed in the center of cavity becomes wider with the increment of *Ra*. Furthermore, the variation of viscosities of shear-thickening fluid ($n = 1.2$) has also been taken into account in the presence of longitudinal wall vibrations, which is shown in Figure 12. In contrast to the shear-thinning fluid, the maximum viscosity of shear-thickening fluid is distributed around the corners of rectangular cavity, and the minimum viscosity is visualized in the central area. As *Ra* increases to 10^5, the area of maximum viscosity has shrunken. In the meantime, the two vortices that are formed in the center of cavity become wider. The viscosity distribution, however, is contrasted with the above situation when the transverse wall vibration is applied (Effect of

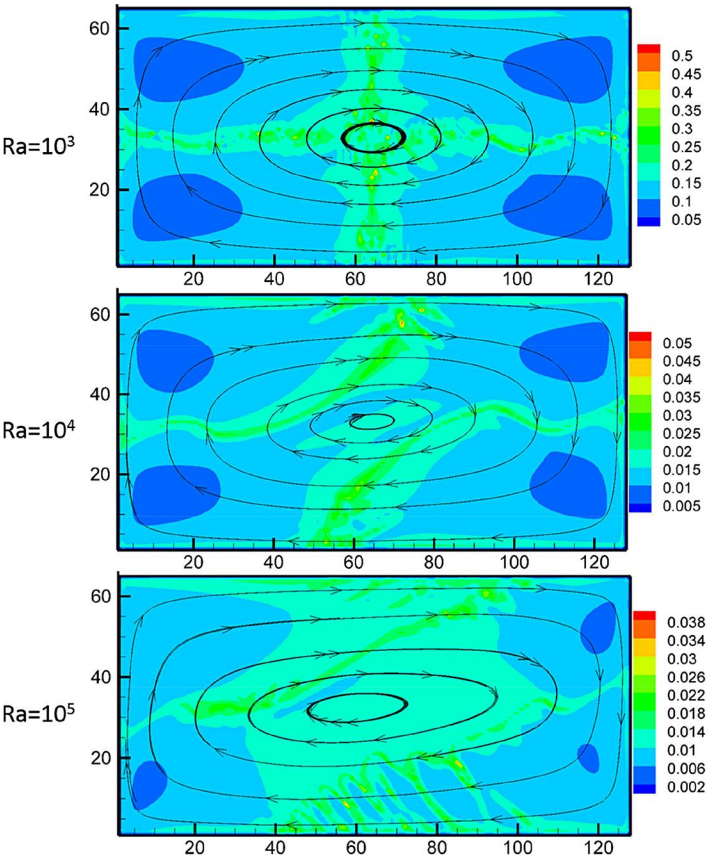

Figure 11. Viscosity contours for the shear-thinning fluid ($n = 0.7$) in a rectangular cavity ($Ra = 10^3$–10^5 and $Pr = 10$) without applying the longitudinal wall vibrations.

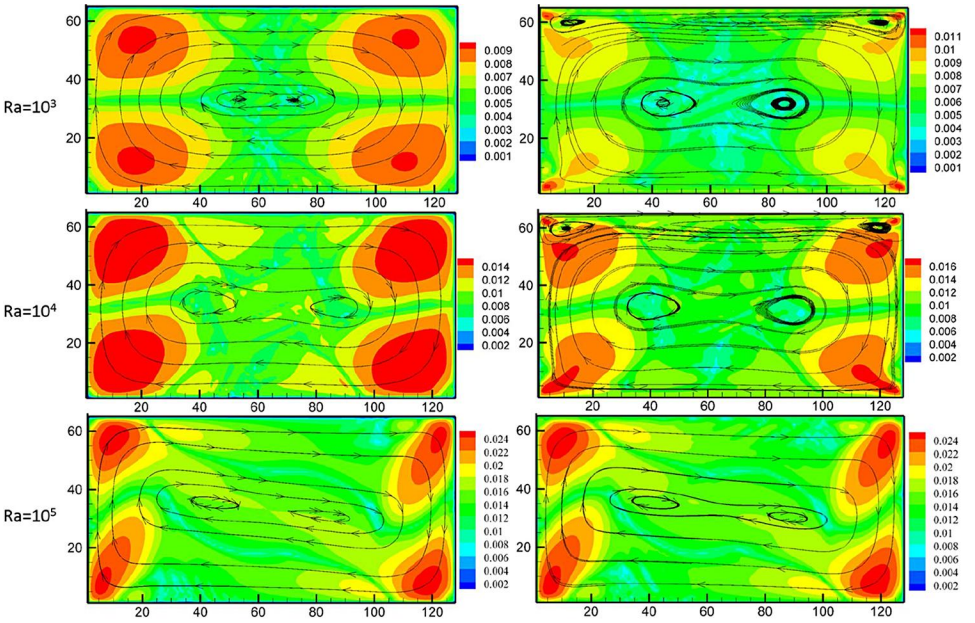

Figure 12. Viscosity contours for the shear-thickening fluid ($n = 1.2$) in a rectangular cavity ($Ra = 10^3$–10^5 and $Pr = 10$), respectively. Left panel: the natural convections without applying the longitudinal wall vibrations. Right panel: the cases in the presence of longitudinal wall vibrations.

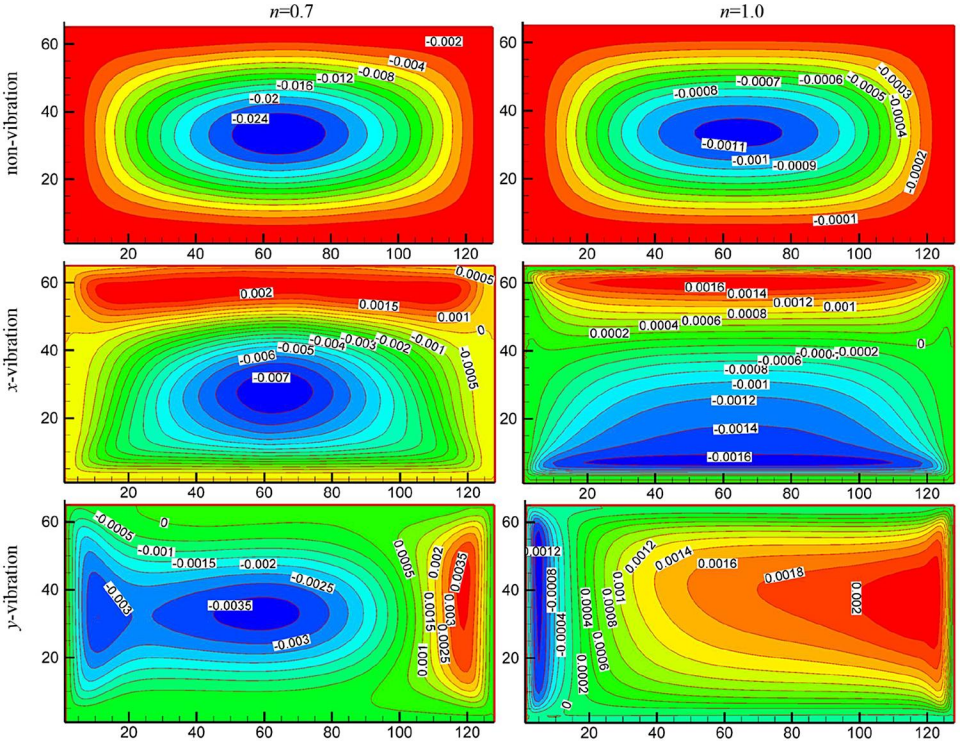

Figure 13. Stream functions of power-law fluids and Newtonian fluid in a rectangular cavity under the longitudinal and transverse vibrations ($Ra = 10^3$ and $Pr = 10$), respectively.

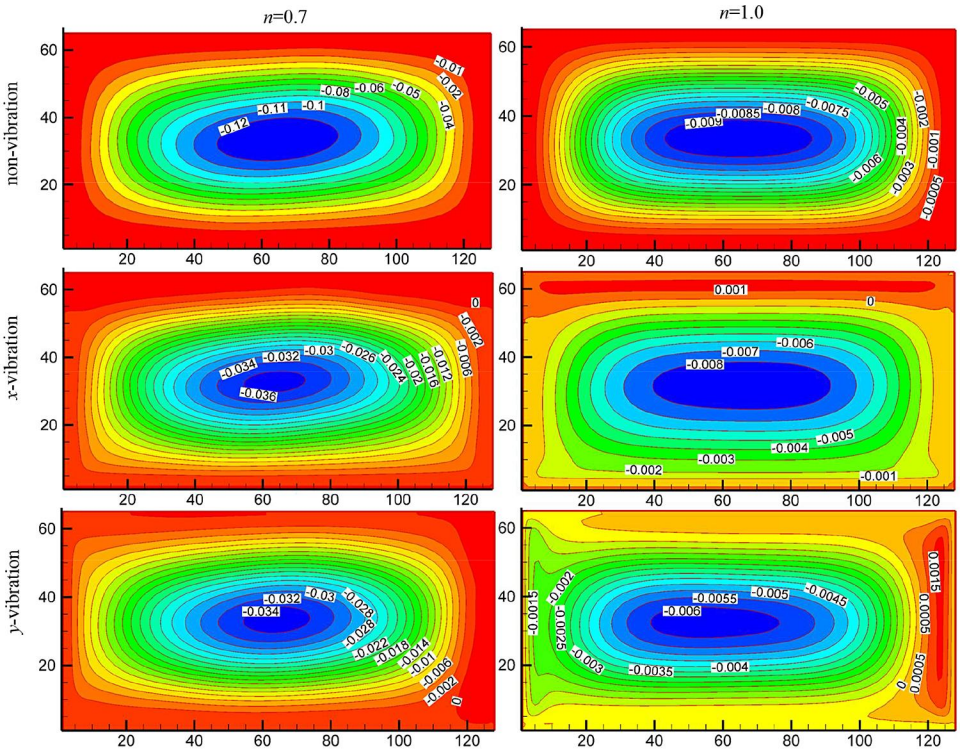

Figure 14. Stream functions of power-law fluids and Newtonian fluid in a rectangular cavity under the longitudinal and transverse vibrations ($Ra = 10^4$ and $Pr = 10$), respectively.

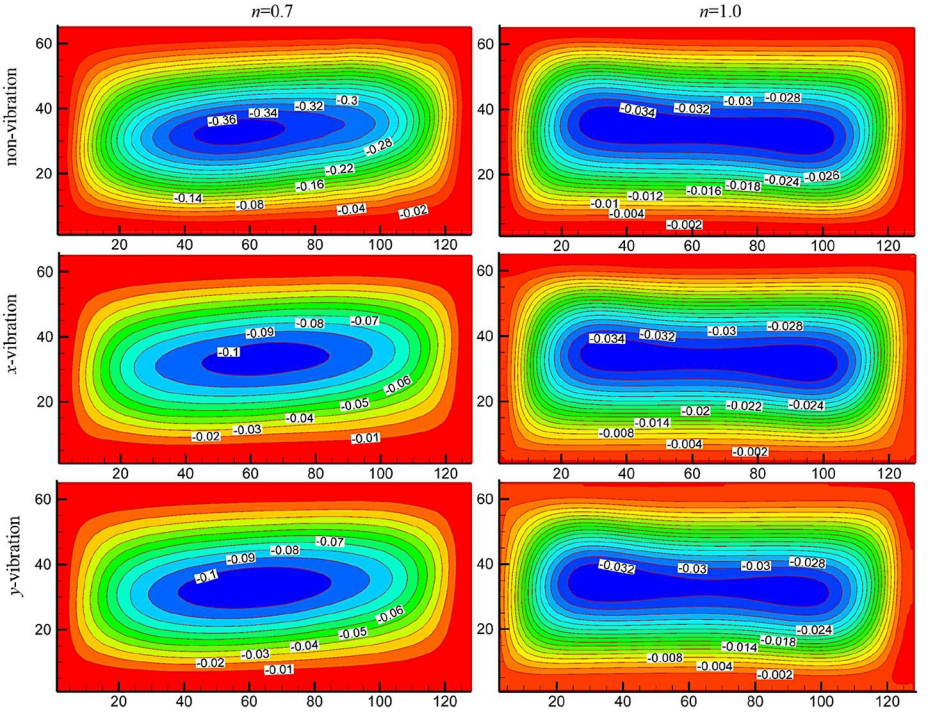

Figure 15. Stream functions of power-law fluids and Newtonian fluid in a rectangular cavity under the longitudinal and transverse vibrations ($Ra = 10^5$ and $Pr = 10$), respectively.

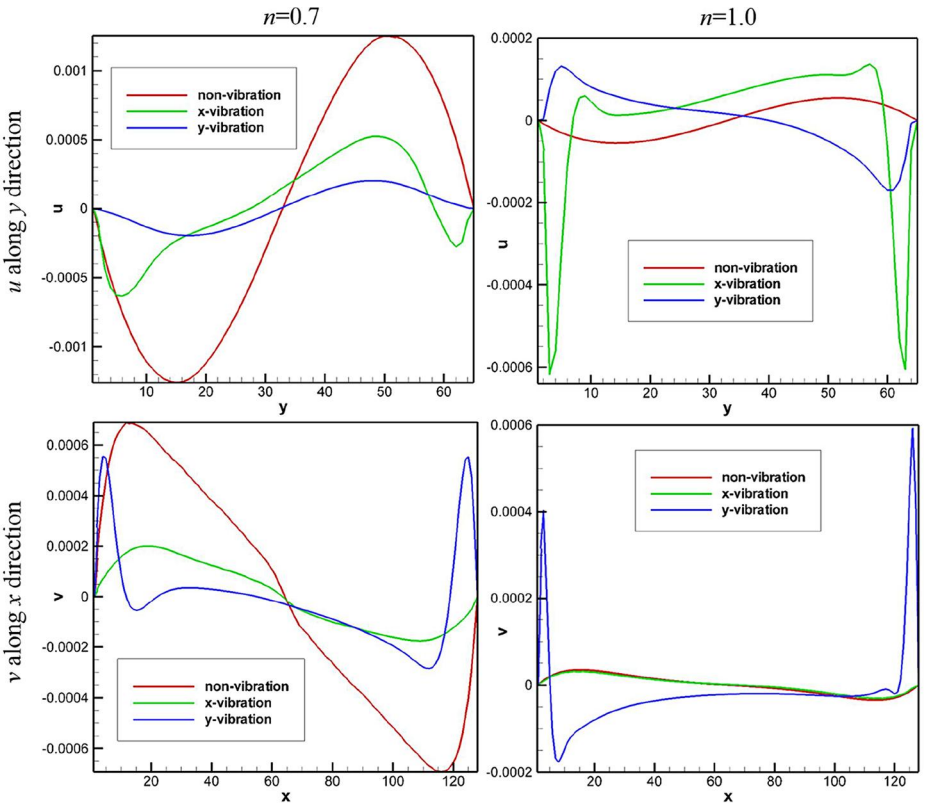

Figure 16. Velocity profiles of power-law fluids and Newtonian fluid at the central line of a rectangular cavity along the *x*- and *y*-directions under the longitudinal and transverse vibrations ($Ra = 10^3$ and $Pr = 10$), respectively.

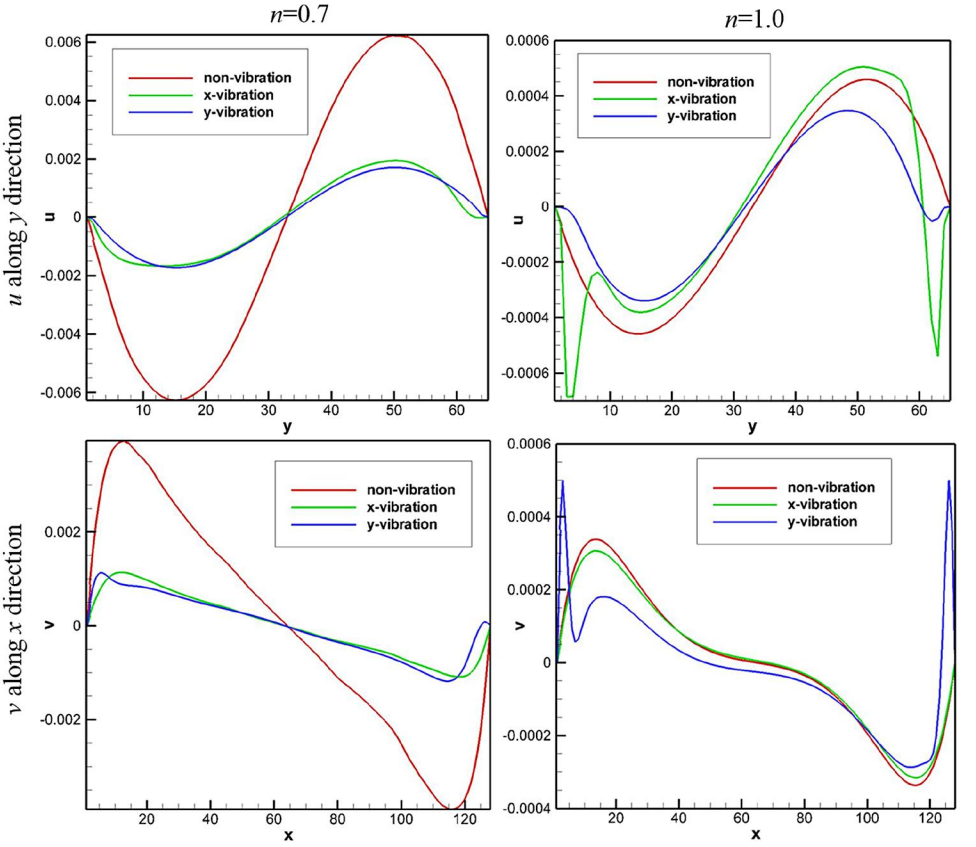

Figure 17. Velocity profiles of power-law fluids and Newtonian fluid at the central line of a rectangular cavity along the *x*- and *y*-directions under the longitudinal and transverse vibrations ($Ra = 10^4$ and $Pr = 10$), respectively.

transverse vibration not shown for brevity.). The area of maximum viscosity is enlarged with the increment of *Ra*, and the two secondary vortices near the top corners have disappeared along with the widening of two main vortices formed in the center of cavity.

Stream functions of power-law fluids are shown in Figures 13–15 for longitudinal and transverse vibrations, respectively. For power-law fluids at $Ra = 10^3$, as shown in Figure 13, the stream function is decreased significantly under the *y*-vibration compared to the *x*-vibration, which are both two orders smaller in magnitude than that without the wall vibration. However, the stream functions are both increased slightly for Newtonian fluid under both *x* and *y*-vibrations. When *Ra* increases to 10^4, as shown in Figure 14, the decrease in stream function for power-law fluid under the *x* and *y*-vibrations is both weakened, which is only one-order smaller in magnitude than that without the wall vibration. Inversely the stream function of Newtonian fluid is decreased slightly under both *x* and *y*-vibrations. As is seen in Figure 15, when *Ra* increases to 10^5, the stream function of power-law fluid is still decreased but keeps the same level as that without the wall vibration. Interestingly the stream function of Newtonian fluid shows no difference under *x*-vibration and slight decrease under *y*-vibration compared to that without the wall vibration.

The velocity profiles of power-law fluids at the central lines of the cavity are tracked illustrating the effect of wall vibration along the longitudinal and transverse directions on the flow, which are shown in Figures 16–18. It is obvious that the velocity components *u* and *v* of power-law fluid at the central line of the cavity have been decreased significantly under wall vibrations at $Ra = 10^3$, particularly under *y*-vibration, as shown in Figure 16. However, the velocity component *u* along the *y*-direction

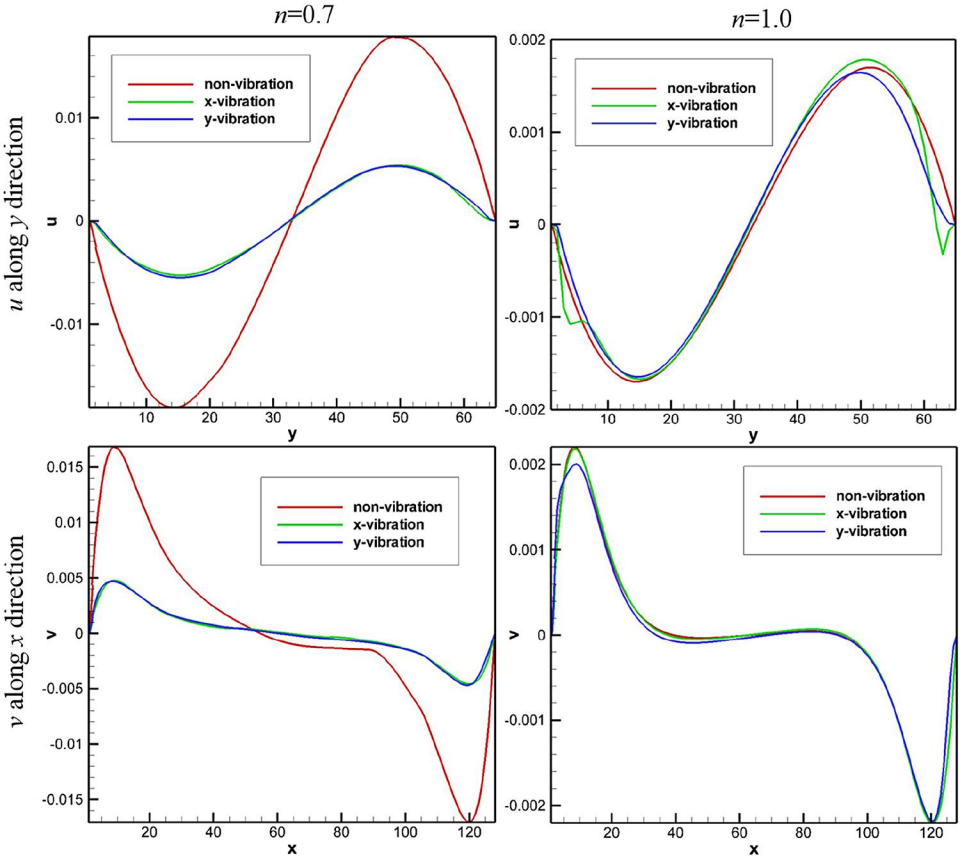

Figure 18. Velocity profiles of power-law fluids and Newtonian fluid at the central line of a rectangular cavity along the *x*- and *y*-directions under the longitudinal and transverse vibrations ($Ra = 10^5$ and $Pr = 10$), respectively.

of Newtonian fluid at the central line of the cavity has been increased under both *x*- and *y*-direction vibrations. The velocity component *v* along *x*-direction under *y*-vibration is larger than that without the vibration, but is the same as that under *x*-vibration. In addition, the velocity components *u* and *v* of Newtonian fluid have been increased sharply near the hot and cool walls under *x* and *y*-vibrations, respectively. Influence of wall vibrations on the velocity components of power-law fluid at the central line of the cavity has been decreased further when *Ra* increases to 10^4, as shown in Figure 17, and the difference between *x*- and *y*-vibrations can be ignored in the main region of the cavity. On the other hand, the effect of wall vibrations on the velocity components of Newtonian fluid is reduced, and the difference between the velocity profiles gets smaller. Besides, the larger velocity component *u* and *v* of Newtonian fluid appears near the hot and cool walls of the cavity under *x*- and *y*-vibrations, respectively. It is seen in Figure 18 that the velocity components of power-law fluid at the central line of the cavity are decreased to the lowest values under wall vibrations and they show no difference between *x*- and *y*-vibrations when *Ra* increases to 10^5. Especially the velocity component *v* along the *x*-direction of power-law fluid has been reduced nearly to zero in the main region of the cavity. That is, the convection of power-law fluid has been "chocked" in the cavity, and the heat transfer has been dominated by conduction. In the meantime, there is no obvious effect of wall vibrations on the velocity components of Newtonian fluid at the central line of cavity at $Ra = 10^5$ whatever the wall vibration is, longitudinal or transverse.

The values for flow parameters of power-law fluids in natural convection such as $\overline{Nu}$, the maximum velocities along the central lines of the cavity U_{max} and V_{max}, and the stream function

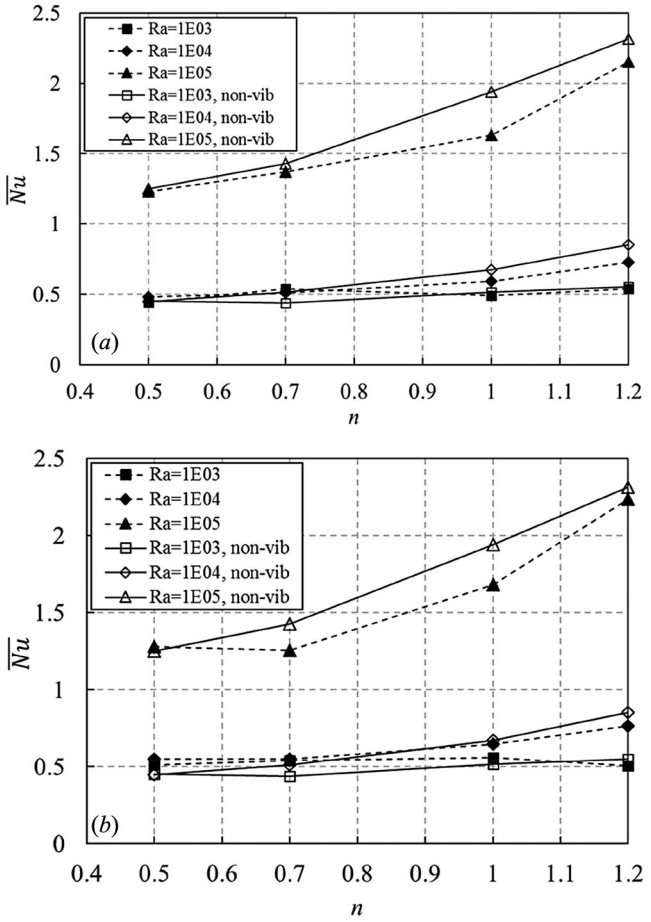

Figure 19. The averaged Nusselt number $\overline{Nu}$ varied as a function of fluid exponent n under the longitudinal (*a*) and transverse (*b*) vibrations ($Pr = 10$ and $Ra = 10^3$, 10^4, 10^5), respectively.

$|\psi_{max}|$ under the longitudinal and transverse vibrations are shown in Tables 4 and 5, respectively. Also, the averaged Nusselt number, maximum velocity components, and the stream function varied as a function of fluid exponent n are plotted in Figures 19–22, respectively. It is seen in Figure 19 that $\overline{Nu}$ is increased significantly with the fluid exponent increasing at $Ra = 10^5$ under both longitudinal and transverse vibrations. In the meantime, the heat transfer rate is smaller under wall vibrations than that without wall vibrations. However, $\overline{Nu}$ is increased slightly at $Ra = 10^4$, and it is kept the level at $Ra = 10^3$. That is, the heat transfer rate is much larger at high Ra than that at low Ra, and the enhancement of heat transfer has been achieved when the heat exchange is dominated by the convection. Therefore, we can conclude that $\overline{Nu}$ increases with Ra increasing for both Newtonian and power-law fluids. Moreover, $\overline{Nu}$ for shear-thinning fluids is greater than that obtained in the case of Newtonian fluids with the same Ra due to strengthening of the convective transport. Turan et al. [65, 66] also found that the effects of convection strengthen with increasing Ra for a given set of fluid exponent n, and with increasing shear-thickening the thermal conduction contributes to the heat transfer principally. In addition, it is shown in Figure 19 that $\overline{Nu}$ increases with Ra increasing in the convection-dominated region, while $\overline{Nu}$ remains approximately constant at low Ra in the conduction-dominated region. This is consistent with the observations in the natural convection of non-Newtonian power-law fluids confined in a cavity with curved vertical walls [67].

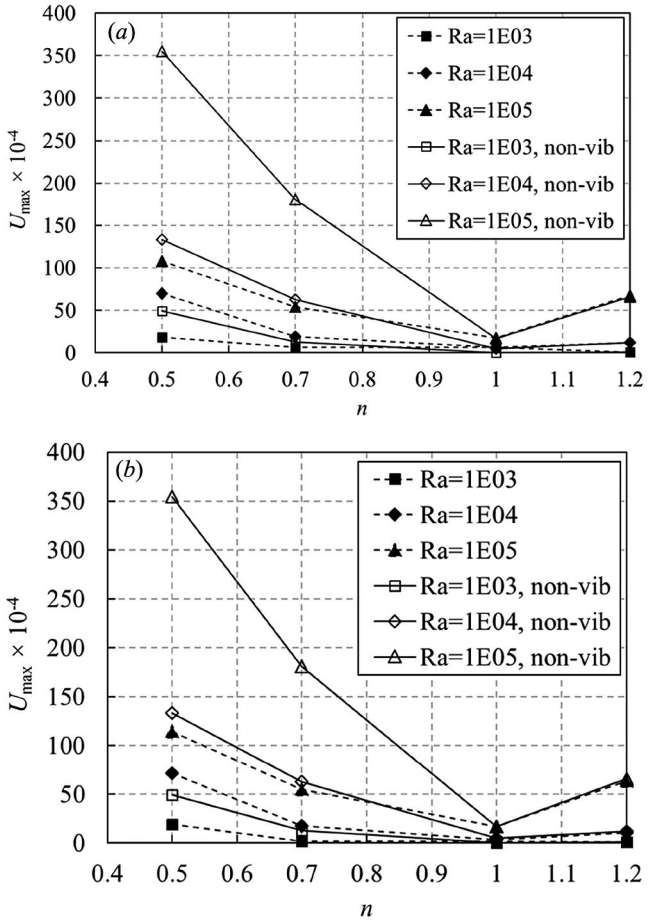

Figure 20. Maximum horizontal component of the velocity U_{max} varied as a function of fluid exponent n under the longitudinal (*a*) and transverse (*b*) vibrations ($Pr = 10$ and $Ra = 10^3$, 10^4, 10^5), respectively.

For the maximum horizontal component of the velocity along the central line of the cavity, as shown in Figure 20, it is decreased under both longitudinal and transverse vibrations as the fluid exponent approaches to unity. However, when the fluid exponent exceeds unity, i.e., the shear-thickening fluid, the maximum horizontal component of the velocity is increased. Particularly, the maximum horizontal component is decreased significantly at $Ra = 10^5$ compared to that at $Ra = 10^3$ and 10^4. It can be explained that the convection has been quenched more sufficiently at large Ra by wall vibrations. Similarly, the maximum vertical component of the velocity along the central line of the cavity is also decreased with the fluid exponent increasing for shear-thinning fluids under both longitudinal and transverse vibrations, which is shown in Figure 21, but it is increased for shear-thickening fluids. It can be also seen that the maximum vertical component has been quenched significantly at $Ra = 10^5$ compared to that at low Ra, which illustrates the same trend as the maximum horizontal component of the velocity of power-law fluids. In addition, it shows no effect of wall vibrations on the maximum velocity components of both Newtonian and shear-thickening fluids. Guha and Pradhan [1] found that the velocity, temperature, and pressure inside the boundary layer depend on the fluid exponent n and Pr, indicating that the shear-thinning fluids show improved heat transfer characteristics as compared to Newtonian and shear-thickening fluids at the same Pr. We have known that the velocity of power-law fluids has been decreased in the middle of the cavity under wall vibrations, and accordingly the variation of stream function as a function of fluid

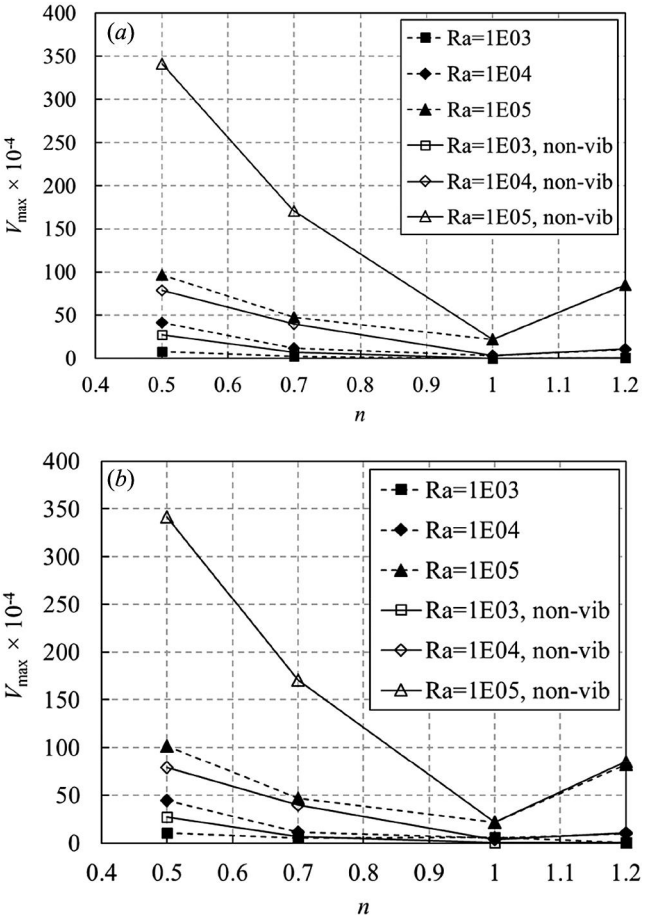

Figure 21. Maximum vertical component of the velocity V_{max} varied as a function of fluid exponent n under the longitudinal (*a*) and transverse (*b*) vibrations ($Pr = 10$ and $Ra = 10^3$, 10^4, 10^5), respectively.

exponent is plotted in Figure 22. It can be seen that the stream function of shear-thinning fluids is decreased significantly under both longitudinal and transverse vibrations at $Ra = 10^5$ compared to that at $Ra = 10^3$ and 10^4. However, wall vibrations have no effect on the stream function of shear-thickening fluids, which is increased with the increase in fluid exponent.

Apart from the fluid exponent and *Ra,* the effect of aspect ratio (AR) on the convective flow and heat transfer has also been taken into account [68, 69], and the results are shown in Table 6 (flow fields not shown for brevity). As is seen in Table 6, $\overline{Nu}$ decreased as the aspect ratio increases, indicating the reduction of heat transfer under longitudinal vibration of horizontal walls. The velocity component of convective flow is affected slightly along the horizontal wall after the AR reaches 2:1, but is reduced dramatically along the vertical wall. Furthermore, the maximum value of stream function is decreased with the increase in AR. The key parameter *Pr* may also play an important role in the natural convection of power-law fluids, and the effect of *Pr* on the convective flow and heat transfer has been investigated, which is shown in Table 7. It is seen in Table 7 that Nu is decreased as *Pr* increases, which indicates that the heat transfer of power-law fluid is weakened at large *Pr* under the longitudinal vibration of horizontal walls. The convective behavior contrasts with that in different aspect ratios, i.e., the velocity component along the horizontal walls is affected significantly by *Pr,* but the component along the vertical walls is changed slightly. However, the variation of maximum value of stream function shows the same trend as AR, and is a decreasing function of *Pr*.

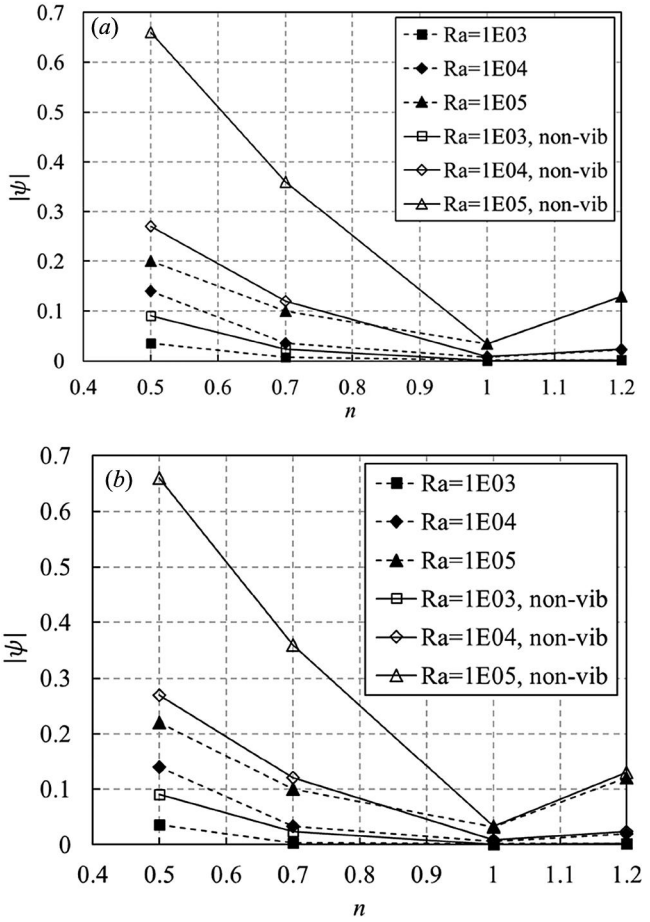

Figure 22. The stream function $|\psi_{max}|$ varied as a function of fluid exponent n under the longitudinal (*a*) and transverse (*b*) vibrations ($Pr = 10$ and $Ra = 10^3$, 10^4, 10^5), respectively.

Table 6. Effect of aspect ratio (AR) on the averaged Nusselt number $\overline{Nu}$, the maximum velocity components along the central lines U_{max}/V^* and V_{max}/V^*, and the stream function $|\psi_{max}|$ under the longitudinal vibration of horizontal walls for $Ra = 10^4$, $Pr = 10$, and $n = 0.7$.

AR	$\overline{Nu}$	U_{max}/V^*	V_{max}/V^*	$\lvert\psi_{max}\rvert$
1:1	1.1171	22.7475	21.6166	0.014
2:1	0.3266	16.6826	5.9659	0.005
3:1	0.2103	15.1419	1.4131	0.0035
4:1	0.1845	16.5949	1.0122	0.002

Table 7. Effect of Prandtl number (*Pr*) on the averaged Nusselt number $\overline{Nu}$, the maximum velocity components along the central lines U_{max}/V^* and V_{max}/V^*, and the stream function $|\psi_{max}|$ under the longitudinal vibration of horizontal walls for $Ra = 10^4$ and $n = 0.7$.

Pr	$\overline{Nu}$	U_{max}/V^*	V_{max}/V^*	$\lvert\psi_{max}\rvert$
2	0.5511	7.6582	4.1683	0.016
4	0.5435	9.5512	4.3023	0.009
6	0.4755	12.1219	4.1385	0.007
8	0.3959	14.5172	4.78263	0.0055
10	0.3266	16.6826	5.9659	0.005
12	0.2991	18.5534	7.3597	0.004

6. Conclusion

The effects of wall vibrations on natural convection of non-Newtonian power-law fluids in a rectangular cavity have been investigated in the frame of lattice Boltzmann scheme. The power-law fluids were heated from the right vertical wall of the cavity and confined between two horizontal walls that vibrated along the longitudinal and transverse directions, respectively. The velocity fields, temperature distributions, and heat transfer characteristics of power-law fluids in the rectangular cavity were influenced by wall vibrations obviously. The averaged Nusselt number near the hot wall was increased significantly with the fluid exponent increasing at high *Ra*. In the meantime, the heat transfer rate was smaller under wall vibrations than that without wall vibrations. However, the averaged Nusselt number was increased slightly at $Ra = 10^4$, and it was kept constant at $Ra = 10^3$, which indicated that the heat transfer rate is much larger at high *Ra* and the enhancement of heat transfer can be achieved when the heat exchange is dominated by the convection. Moreover, wall vibrations showed slight and even no influence on the averaged Nusselt number of power-law fluids at low *Ra*.

The velocity components along the central lines of the cavity were decreased significantly for power-law fluids under wall vibrations. However, it showed no influence on the Newtonian fluid. The maximum velocity components of shear-thinning fluids were both decreased under wall vibrations with the fluid exponent increasing, but it was unchanged in shear-thickening fluids. For the maximum horizontal component of the velocity along the central line of the cavity, it was decreased under both longitudinal and transverse vibrations as the fluid exponent approached to unity. However, when the fluid exponent was greater than unity, i.e., the shear-thickening fluid, the maximum horizontal component of the velocity was increased. Particularly, the maximum horizontal component was decreased significantly at $Ra = 10^5$ compared to that at $Ra = 10^3$ and 10^4, which indicated that the convection was quenched more sufficiently by wall vibrations at large *Ra*. In addition, it showed no effect of wall vibrations on the maximum velocity components of both Newtonian and shear-thickening fluids. The similar situation happened to the maximum vertical component of the velocity along the central line of the cavity. Correspondingly, the stream function of shear-thinning fluids was decreased under wall vibrations, indicating the weakening of convection. However, wall vibrations had no effect on the stream function of shear-thickening fluids, which was increased with the fluid exponent increasing. It can be concluded that the effects of wall vibrations on the streamlines, isotherm contours and heat transfer characteristics of power-law fluids have been observed obviously at high *Ra* ($\sim 10^5$). The effects of AR and *Pr* were also taken into account, and the heat transfer rate was decreased with the increment of both AR and *Pr*.

Funding

We wish to acknowledge the financial support of National Natural Science Foundation of China (Grants No. 51506110 and 51676108) and Science Fund for Creative Research Groups (No. 51621062) for this work. Jian-Fei Xie also thanks China Postdoctoral Science Foundation (Grant No. 2015M581090) for the support.

References

[1] A. Guha and K. Pradhan, "Natural convection of non-Newtonian power-law fluids on a horizontal plate," *Int. J. Heat Mass Transfer*, vol. 70, pp. 930–938, 2014.
[2] I. Vinogradov, L. Khezzar, and D. Siginer, "Heat transfer of non-Newtonian dilatant power law fluids in square and rectangular cavities," *J. Appl. Fluid Mech.*, vol. 4, pp. 37–42, 2011.
[3] M. Sairamu and R. Chhabra, "Natural convection in power-law fluids from a tilted square in an enclosure," *Int. J. Heat Mass Transfer*, vol. 56, no. 12, pp. 319–339, 2013.
[4] T. Zhang and D. Che, "Lattice Boltzmann simulation of natural convection in an inclined square cavity with spatial temperature variation," *Numer. Heat Transfer A Appl.*, vol. 66, no. 6, pp. 712–732, 2014.
[5] G. R. Kefayati, "Simulation of ferrofluid heat dissipation effect on natural convection at an inclined cavity filled with kerosene/cobalt utilizing the lattice Boltzmann method," *Numer. Heat Transfer A*, vol. 65, no. 6, pp. 509–530, 2014.

[6] M. E. Abdallaoui, M. Hasnaoui, and A. Amahmid, "Lattice-Boltzmann modeling of natural convection between a square outer cylinder and an inner isosceles triangular heating body," *Numer. Heat Transfer A*, vol. 66, no. 9, pp. 1076–1096, 2014.
[7] G. Kefayati, "FDLBM simulation of magnetic field effect on natural convection of non-Newtonian power-law fluids in a linearly heated cavity," *Powder Technol.*, vol. 256, pp. 87–99, 2014.
[8] G. Kefayati, "{FDLBM} simulation of entropy generation due to natural convection in an enclosure filled with non-Newtonian nanofluid," *Powder Technol.*, vol. 273, pp. 176–190, 2015.
[9] G. Kefayati, "Simulation of heat transfer and entropy generation of MHD natural convection of non-Newtonian nanofluid in an enclosure," *Int. J. Heat Mass Transfer*, vol. 92, pp. 1066–1089, 2016.
[10] G. Kefayati, "Mesoscopic simulation of double-diffusive mixed convection of pseudoplastic Fluids in an enclosure with sinusoidal boundary conditions," *Comput. Fluids*, vol. 97, pp. 94–109, 2014.
[11] G. Kefayati, "Mixed convection of non-Newtonian nanofluids flows in a lid-driven enclosure with sinusoidal temperature profile using {FDLBM}," *Powder Technol.*, vol. 266, pp. 268–81, 2014.
[12] N. Vasu and S. De, "Electroviscous effects in purely pressure driven flow and stationary plane analysis in electroosmotic flow of power-law fluids in a slit microchannel," *Int. J. Eng. Sci.*, vol. 48, pp. 1641–1658, 2010.
[13] D. Lacitignola and G. Saccomandi, "An anomalous feature in a semi-inverse solution of a simple model of non-Newtonian fluid mechanics," *Int. J. Eng. Sci.*, vol. 60, pp. 94–98, 2012.
[14] P. S. Gnambode, P. Orlandi, M. Ould-Rouiss, and X. Nicolas, "Large-Eddy simulation of turbulent pipe flow of (power-law) fluids," *Int. J. Heat Fluid Flow*, vol. 54, pp. 196–210, 2015.
[15] J. M. Nouri and J. H. Whitelaw, "Flow of Newtonian and non-Newtonian fluids in an eccentric annulus with rotation of the inner cylinder," *Int. J. Heat Fluid Flow*, vol. 18, pp. 236–246, 1997.
[16] M. P. Escudier, P. J. Oliveira, and F. T. Pinho, "Fully developed laminar flow of purely viscous non-Newtonian liquids through annuli, including the effects of eccentricity and inner-cylinder rotation," *Int. J. Heat Fluid Flow*, vol. 23, pp. 52–73, 2002.
[17] M. M. Alam and S. Kim, "Free vibration of two identical circular cylinders in staggered arrangement," *Fluid Dyn. Res.*, vol. 41, p. 035507, 2009.
[18] M. Zhao, "Flow-induced vibrations of square and rectangular cylinders at low Reynolds number," *Fluid Dyn. Res.*, vol. 47, p. 025502, 2015.
[19] M. Eesa and M. Barigou, "CFD analysis of viscous non-Newtonian flow under the influence of a superimposed rotational vibration," *Comput. Fluids*, vol. 37, pp. 24–34, 2008.
[20] F. J. Higuera and S. Succi, "Simulating the flow around a circular cylinder with a lattice Boltzmann equation," *Europhys. Lett.*, vol. 8, p. 517, 1989.
[21] F. J. Higuera, S. Succi, and R. Benzi, "Lattice gas dynamics with enhanced collisions," *Europhys. Lett.*, vol. 9, pp. 345–349, 1989.
[22] S. Chen and G. D. Doolen, "Lattice Boltzmann method for fluid flows," *Ann. Rev. Fluid Mech.*, vol. 30, pp. 329–364, 1998.
[23] C. Succi, *Lattice Boltzmann equation for fluid dynamics and beyond*. Oxford: Clarendon Press, 2001.
[24] J.-F. Xie, S. He, Y. Q. Zu, B. Lamy-Chappuis, and B. W. D. Yardley, "Relative permeabilities of supercritical CO_2 and brine in carbon sequestration by a two-phase lattice Boltzmann method," *Heat Mass Transfer*, vol. 53, no. 8, pp. 2637–2649, 2017.
[25] X. He, S. Chen, and G. D. Doolen, "A novel thermal model for the lattice Boltzmann method in incompressible limit," *J. Compt. Phys.*, vol. 146, pp. 282–300, 1998.
[26] C. Zhong, J. Xie, C. Zhuo, S. Xiong, and D. Yin, "Simulation of natural convection under high magnetic field by means of the thermal lattice Boltzmann method," *Chin. Phys. B*, vol. 18, pp. 4083–4093, 2009.
[27] F. Meng, M. Wang, and Z. Li, "Lattice Boltzmann simulations of conjugate heat transfer in high-frequency oscillating flows," *Int. J. Heat Fluid Flow*, vol. 29, pp. 1203–1210, 2008.
[28] H. Başağaoğlu, C. T. Green, P. Meakin, and B. J. McCoy, "Lattice-Boltzmann simulation of coalescence-driven island coarsening," *J. Chem. Phys.*, vol. 121, pp. 7987–7995, 2004.
[29] M. R. Kamali, J. J. J. Gillissen, H. E. A. van den Akker, and S. Sundaresan, "Lattice Boltzmann-based two-phase thermal model for simulating phase change," *Phys. Rev. E*, vol. 88, p. 033302, 2013.
[30] T. Shi, W. Liang, and G. Zhao-Li, "Lattice Boltzmann modeling of microscale oscillating Couette flow," *Acta Phys. Sin.*, vol. 63, p. 214703, 2014.
[31] E. Aharonov and D. H. Rothman, "Non-Newtonian flow (through porous-media)—A Lattice-Boltzmann method," *Geophys. Res. Lett.*, vol. 20, pp. 679–682, 1993.
[32] S. Gabbanelli, G. Drazer, and J. Koplik, "Lattice Boltzmann method for non-Newtonian (power-law) fluids," *Phys. Rev. E*, vol. 72, p. 046312, 2005.
[33] S. Zou, X.-F. Yuan, X. Yang, W. Yi, and X. Xu, "An integrated lattice Boltzmann and finite volume method for the simulation of viscoelastic fluid flows," *J. Non-Newtonian Fluid Mech.*, vol. 211, pp. 99–113, 2014.
[34] L. Wang, J. Mi, X. Meng, and Z. Guo, "A localized mass-conserving lattice Boltzmann approach for non-Newtonian fluid flows," *Commun. Comput. Phys.*, vol. 17, pp. 908–924, 2015.

[35] Y. Wang, C. Shu, L. Yang, and H. Yuan, "A decoupling multiple-relaxation-time lattice Boltzmann flux solver for non-Newtonian power-law fluid flows," *J. Non-Newtonian Fluid Mech.*, vol. 235, pp. 20–28, 2016.
[36] C. Xie, J. Zhang, V. Bertola, and M. Wang, "Lattice Boltzmann modeling for multiphase viscoplastic fluid flow," *J. Non-Newtonian Fluid Mech.*, vol. 234, pp. 118–128, 2016.
[37] M. Yoshino, Y. Hotta, T. Hirozane, and M. Endo, "A numerical method for incompressible non-Newtonian fluid flows based on the lattice Boltzmann method," *J. Non-Newtonian Fluid Mech.*, vol. 147, pp. 69–78, 2007.
[38] C.-H. Wang and J.-R. Ho, "Lattice Boltzmann modeling of Bingham plastics," *Phys. A*, vol. 387, pp. 4740–4748, 2008.
[39] C.-H. Wang and J.-R. Ho, "A lattice Boltzmann approach for the non-Newtonian effect in the blood flow," *Comput. Math. Appl.*, vol. 62, pp. 75–86, 2011.
[40] A. A. Delouei, M. Nazari, M. Kayhani, S. Kang, and S. Succi, "Non-Newtonian particulate flow simulation: A direct-forcing immersed boundary lattice Boltzmann approach," *Phys. A*, vol. 447, pp. 1–20, 2016.
[41] A. A. Delouei, M. Nazari, M. H. Kayhani, and S. Succi, "Non-Newtonian unconfined flow and heat transfer over a heated cylinder using the direct-forcing immersed boundary ?thermal lattice Boltzmann method," *Phys. Rev. E*, vol. 89, p. 053312, 2014.
[42] A. A. Delouei, M. Nazari, M. H. Kayhani, and S. Succi, "Immersed boundary thermal lattice Boltzmann methods for non-Newtonian flows over a heated cylinder: A comparative study," *Comm. Compt. Phys.*, vol. 18, pp. 489–515, 2014.
[43] A. De Rosis, "Harmonic oscillations of laminae in non-Newtonian fluids: A lattice Boltzmann-immersed boundary approach," *Adv. Water Res.*, vol. 73, pp. 97–107, 2014.
[44] Y. H. Qian, D. Dhumieres, and P. Lallemand, "Lattice BGK models for Navier–Stokes equation," *Europhys. Lett.*, vol. 17, pp. 479–484, 1992.
[45] M. Wang, J. Wang, and S. Chen, "Roughness and cavitation effects on electro-osmotic flows in rough microchannels using the lattice Poisson–Boltzmann methods," *J. Compt. Phys.*, vol. 226, pp. 836–851, 2007.
[46] U. Frisch *et al.*, "Lattice gas hydrodynamics in two and three dimensions," *Complex Syst.*, vol. 1, p. 6491707, 1987.
[47] B. Chopard and M. Droz, *Cellular automata modeling of physical systems*. Cambridge: Cambridge University Press, 1998.
[48] W. Wilkenson, *Non-Newtonian fluids, fluid mechanics, mixing and heat transfer*. London: Pergamon Press, 1960.
[49] J. M. Piau and M. Piau, "Easier flow of viscoplastic materials with ultrasonic longitudinal wall motion," *J. Non-Newtonian Fluid Mech.*, vol. 104, pp. 185–226, 2002.
[50] M. Piau and J. M. Piau, "Plane Couette flow of viscoplastic materials along a slippery vibrating wall," *J. Non-Newtonian Fluid Mech.*, vol. 125, pp. 71–85, 2005.
[51] J. M. Piau and M. Piau, 'Wall vibration and yield stress-shear thinning coupling (small vibration inertia)," *J. Non-Newtonian Fluid Mech.*, vol. 144, pp. 59–72, 2007.
[52] G. Kim, J. Hyun, and H. Kwak, "Transient buoyant convection of a power-law non-Newtonian fluid in an enclosure," *Int. J. Heat Mass Transfer*, vol. 46, pp. 3605–3617, 2003.
[53] J. Boyd, J. Buick, and S. Green, "A second-order accurate lattice Boltzmann non-Newtonian flow model," *J. Phys. A Math. Gen.*, vol. 39, pp. 14241–14247, 2006.
[54] Y. Peng, C. Shu, and Y. Chew, "A 3d incompressible thermal lattice Boltzmann model and its application to simulate natural convection in a cubic cavity," *J. Compt. Phys.*, vol. 193, pp. 260–274, 2004.
[55] C. van Treeck, E. Rank, M. Krafczyk, J. Tolke, and B. Nachtwey, "Extension of a hybrid thermal LBE scheme for large-eddy simulations of turbulent convective flows," *Comput. Fluids*, vol. 35, pp. 863–871, 2006.
[56] Z. Guo, C. Zheng, and B. Shi, "Non-equilibrium extrapolation method for velocity and pressure boundary conditions in the lattice Boltzmann method," *Chin. Phys.*, vol. 11, pp. 366–374, 2002.
[57] S. Chen, D. Martnez, and R. Mei, "On boundary conditions in lattice Boltzmann methods," *Phys. Fluids*, vol. 8, pp. 2527–2536, 1996.
[58] Z. Guo, C. Zheng, and B. Shi, "An extrapolation method for boundary conditions in lattice Boltzmann method," *Phys. Fluids*, vol. 14, pp. 2007–2010, 2002.
[59] H. P. Fang, Z. W. Wang, Z. F. Lin, and M. R. Liu, "Lattice Boltzmann method for simulating the viscous flow in large distensible blood vessels," *Phys. Rev. E*, vol. 65, p. 051925, 2002.
[60] O. Behrend, R. Harris, and P. B. Warren, "Hydrodynamic behavior of lattice Boltzmann and lattice Bhatnagar-Gross-Krook models," *Phys. Rev. E*, vol. 50, pp. 4586–4595, 1994.
[61] X. D. Niu, C. Shu, Y. T. Chew, and T. G. Wang, "Investigation of stability and hydrodynamics of different Lattice Boltzmann models," *J. Stat. Phys.*, vol. 117, pp. 665–680, 2004.
[62] J. Eggels and J. Somers, "Numerical simulation of free convective flow using the Lattice-Boltzmann scheme," *Int. J. Heat Fluid Flow*, vol. 16, pp. 357–364, 1995.
[63] Q. S. Zou and X. Y. He, "On pressure and velocity boundary conditions for the lattice Boltzmann BGK model," *Phys. Fluids*, vol. 9, pp. 1591–1598, 1997.
[64] J. Psihogios, M. E. Kainourgiakis, A. G. Yiotis, A. T. Papaioannou, and A. K. Stubos, "A lattice Boltzmann study of non-Newtonian flow in digitally reconstructed porous domains," *Trans. Porous Media*, vol. 70, pp. 279–292, 2007.

[65] O. Turan, A. Sachdeva, N. Chakraborty, and R. J. Poole, "Laminar natural convection of power-law fluids in a square enclosure with differentially heated side walls subjected to constant temperatures," *J. Non-Newtonian Fluid Mech.*, vol. 166, pp. 1049–1063, 2011.
[66] O. Turan, J. Lai, R. J. Poole, and N. Chakraborty, "Laminar natural convection of power-law fluids in a square enclosure submitted from below to a uniform heat flux density," *J. Non-Newtonian Fluid Mech.*, vol. 199, pp. 80–95, 2013.
[67] C.-C. Cho, C.-L. Chen, J.-J. Hwang, and C.-K. Chen, "Natural convection heat transfer performance of non-Newtonian power-law fluids enclosed in cavity with complex-wavy surfaces," *J. Heat Transfer ASME*, vol. 136, p. 014502, 2014.
[68] G. G. Ilis, M. Mobedi, and B. Sunden, "Effect of aspect ratio on entropy generation in a rectangular cavity with differentially heated vertical walls," *Int. Comm. Heat Mass Transfer*, vol. 35, pp. 696–703, 2008.
[69] L. Khezzar, D. Siginer, and I. Vinogradov, "Natural convection of power law fluids in inclined cavities," *Int. J. Therm. Sci.*, vol. 53, pp. 8–17, 2012.
[70] G. Barakos, E. Mitsoulis, and D. Assimacopoulos, "Natural convection flow in a square cavity revisited: Laminar and turbulent models with wall functions," *Int. J. Numer. Methods Fluids*, vol. 18, pp. 695–719, 1994.
[71] G. de Vahl Davis and I. P. Jones, "Natural convection in a square cavity: A comparison exercise," *Int. J. Numer. Methods Fluids*, vol. 3, pp. 227–248, 1983.
[72] T. Fusegi, J. Hyun, K. Kuwahara, and B. Farouk, A numerical study of three-dimensional natural convection in a differentially heated cubical enclosure, *Int. J. Heat Mass Transfer*, vol. 34, pp. 1543–1557, 1991.
[73] R. J. A. Janssen, "Instabilities in natural-convection flows in cavities," PhD thesis, Technische Hogeschool Delft, Netherlands, 1994.
[74] P. Le Quéré, "Accurate solutions to the square thermally driven cavity at high Rayleigh number," *Comput. Fluids*, vol. 20, pp. 29–41, 1991.